

Topology-preserving Scan-based Immersed Isogeometric Analysis

Sai C Divi^{a,b,*}, Clemens V Verhoosel^a, Ferdinando Auricchio^b, Alessandro Reali^b,
E Harald van Brummelen^a

^a*Department of Mechanical Engineering, Eindhoven University of Technology, 5600MB Eindhoven, The Netherlands*

^b*Department of Civil Engineering and Architecture, University of Pavia, 27100 Pavia, Italy*

Abstract

To exploit the advantageous properties of isogeometric analysis (IGA) in a scan-based setting, it is important to extract a smooth geometric domain from the scan data (*e.g.*, voxel data). IGA-suitable domains can be constructed by convoluting the grayscale data using B-splines. A negative side-effect of this convolution technique is, however, that it can induce topological changes in the process of smoothing when features with a size similar to that of the voxels are encountered. This manuscript presents an enhanced B-spline-based segmentation procedure using a refinement strategy based on truncated hierarchical (TH)B-splines. A Fourier analysis is presented to explain the effectiveness of local grayscale function refinement in repairing topological anomalies. A moving-window-based topological anomaly detection algorithm is proposed to identify regions in which the grayscale function refinements must be performed. The criterion to identify topological anomalies is based on the Euler characteristic, giving it the capability to distinguish between topological and shape changes. The proposed topology-preserving THB-spline image segmentation strategy is studied using a range of test cases. These tests pertain to both the segmentation procedure itself, and its application in an immersed IGA setting.

Keywords: Scan-based analysis, Isogeometric analysis (IGA), Finite Cell Method (FCM), Image filtering, Topology detection

*Corresponding author

Email addresses: s.c.divi@tue.nl (Sai C Divi), C.V.Verhoosel@tue.nl (Clemens V Verhoosel), auricchio@unipv.it (Ferdinando Auricchio), alessandro.reali@unipv.it (Alessandro Reali), E.H.v.Brummelen@tue.nl (E Harald van Brummelen)

1. Introduction

Computational analyses based on volumetric scan data are of interest in many fields of research, such as biomechanics, geomechanics, material science, microstructural analysis, and many more. Scan-based simulations are inherently three-dimensional and, frequently, the computational domains are complex, both in terms of geometry and in terms of topology. In addition, the data sets obtained from, *e.g.*, tomography or photogrammetry techniques are large in size and represented in data formats which are not directly suitable for analysis (*e.g.*, DICOM¹, NIFTI²). For these reasons, performing high-fidelity simulations at practical computational costs is still very challenging.

Over the past decade, the use of Isogeometric Analysis (IGA) [1] to perform accurate scan-based simulations at acceptable computational costs has been explored. Originally, IGA was proposed as an analysis paradigm to better integrate analysis and design by employing the spline basis functions from Computer Aided Design (CAD) directly for the analysis, without intermediate geometry clean-up and meshing operations [2], as required in traditional finite element analyses. The advantageous properties of spline basis functions, in particular their higher-order regularity, have made IGA also attractive for simulations where the geometry is not represented by a CAD model [3–6]. In the context of scan-based isogeometric analysis, the usage of standard discretization techniques such as the voxel method [7] or (unstructured) conforming mesh approaches (*e.g.*, generated using a marching cube algorithm [8, 9]) is not possible, as this deteriorates the favorable properties of IGA. Therefore, various enhanced isogeometric techniques for scan-based analysis have been developed. These can be summarized as follows:

- **Template-fitting techniques** construct a spline-based template geometry (typically consisting of multiple patches) that captures the essential features of the scanned object, and subsequently apply fitting procedures to reposition the control points of the template to match the scan data. An advantage of such techniques is that an explicit parametrization of the scan object is retrieved, which is beneficial from an analysis point of view. The downside of template fitting techniques is that they are not useful in cases where the topology of the object is not known *a priori*. For cases where the topology of the object is known but complex, template fitting techniques are typically laborious. Template fitting techniques using IGA have, for example, been applied to fluid-structure interaction analyses of arterial blood flow [10, 11], patient-specific blood-flow analyses in arteries [3, 12] (see [13] for a review), the mechanical behavior of a femur (consisting of both hard outer cortical bone and inner trabecular bone) [14], the mechanical behavior of a carotid artery stent [15], damage in composite laminates [16], the human heart [17], and fluid-structure interactions of a heart valve [18].
- **Immersed methods** construct a structured mesh for the entire scan domain, typically a box, and then represent the scanned object by an inside/outside relation to indicate whether a specific point in the box is part of the object. In the context of scan-based analysis, the inside/outside relation can directly be retrieved from the scan data (intensity) in the form of a level set function [19], but the immersed concept can also be applied to obtain volumetric representations of objects identified by boundary representations (*e.g.*, BREP [20–25], STL³ [26–30]) and to represent trimming operations in CAD models (*e.g.*, [31–33]). The advantage of immersed techniques is their versatility with respect to the geometry and topology of the scanned objects, in the sense that the analysis procedure is not essentially affected by increasing the complexity of the objects. From an analysis perspective, the immersed approach poses additional challenges compared to mesh-fitting analyses. Most notably, numerical integration of trimmed elements is challenging from an efficiency point of view, application of boundary conditions can be non-standard, and the system of equations is generally ill-conditioned without dedicated treatment. Immersed scan-based IGA has, for example, been applied for the analysis of trabecular bone [19, 22, 34], coated metal foams [35], porous media [36], metal castings [37] and in additive manufacturing [38].

¹Digital Imaging and Communications in Medicine

²Neuroimaging Informatics Technology Initiative

³Standard Triangle Language or Standard Tessellation Language

The choice for either a template-fitting technique or an immersed technique is to a large extent dictated by the topological complexity of the scanned object. If a template with a reasonably low number of control points can be constructed for the object of interest, template-fitting is generally favorable. If the creation of a template is impractical, immersed methods are preferred. It should be noted that it can be favorable to combine the two techniques for particular scan-based analyses, to exploit the advantages of both of them. A noteworthy example in this regard is the heart-valve problem by Kamensky *et al.* [39–41], where the heart chambers are modeled through a template-fitting approach, and the moving valves through an immersed approach.

In this work we build on the immersed scan-based analysis framework originally proposed in Ref. [19]. In recent years, significant progress has been made to tackle the above-mentioned challenges associated with immersed methods. A myriad of advanced integration techniques has been developed to reduce the computational burden associated with the integration of trimmed elements; see, *e.g.*, Refs. [42–45]. Nitsche’s method [46] has been demonstrated to be a reliable technique to impose essential boundary conditions along immersed boundaries, *e.g.*, [23, 47–49], and various techniques have been developed to construct a parametrization of immersed boundaries to impose boundary conditions [49–52]. With respect to the stability and conditioning, fundamental understanding was obtained in Refs. [23, 53], and various types of remedies have been demonstrated to be effective, see, *e.g.*, [5, 36, 37, 50, 51, 54–58]. The various advancements of immersed techniques have made it into a versatile technique for scan-based analyses, being able to model problems in different physical domains (solid mechanics, fluid dynamics), considering high-performance computing problems [19, 26, 34, 36, 37, 42, 59, 60], and being applicable in the context of highly nonlinear problems [61–64].

Although immersed isogeometric analysis is very flexible with respect to capturing topologically complex volumetric objects, topological anomalies associated with the image segmentation procedure can occur [65–69]. This is specifically the case when the resolution of the scan data is only nearly sufficient to capture the smallest features in the scanned object. Image smoothing operations, in the case of the procedure of Ref. [19] associated with the order of the spline level set construction, can trigger undesirable topology alterations (*e.g.*, closure of a channel, (dis)connection of structures). The occurrence of topological anomalies associated with smoothing operations is well understood in the field of image segmentation (*e.g.*, [70–73]). Various enhanced image-segmentation techniques have been proposed in order to ameliorate such problems, like homology-based preservation techniques [74–80], topology-derivative-based techniques [81–85], and adaptive refinement techniques [72, 86–91].

In this contribution we propose an enhancement of the immersed isogeometric analysis framework of Ref. [19] that rigorously avoids the occurrence of topological anomalies associated with the B-spline-based image segmentation procedure. The filtering analysis in Ref. [19] is extended to include the effect of the level set mesh size. Based on this analysis, it is proposed to employ truncated hierarchical B-splines (THB-splines) [92–94] to discretize the grayscale intensity of the scan data. Inspired by topology characteristics (*e.g.*, Betti numbers, Euler characteristic) to detect local topology anomalies [77, 78, 95–97], this local refinement capability for the level set representation is complemented with an Euler characteristic evaluation and moving-window technique to detect local topology anomalies. The resulting topology-preserving immersed isogeometric analysis is demonstrated using prototypical test cases in two and three dimensions, considering both the image-segmentation problem and the complete (stabilized) immersed isogeometric analysis problem [36]. A scan-based analysis on a representative data set is considered to demonstrate the practical applicability of the proposed technique. In this contribution, we restrict ourselves to user-specified locally-refined meshes, keeping in mind the extension to an adaptive analysis framework as a possible further development.

This paper is organized as follows. In Section 2 we first extend the filtering analysis of Ref. [19]. Based on this analysis, in Section 3 we introduce the topology-preserving extension of the spline-based image segmentation technique. This technique comprises the moving-window technique to detect topological anomalies (Section 3.1) and a THB-spline-based discretization of the level set function (Section 3.2). The adopted immersed isogeometric analysis framework, including stabilization techniques, is introduced in Section 4. Numerical examples are then presented in Section 5 to test the proposed technique. Finally, conclusions and recommendations are drawn in Section 6.

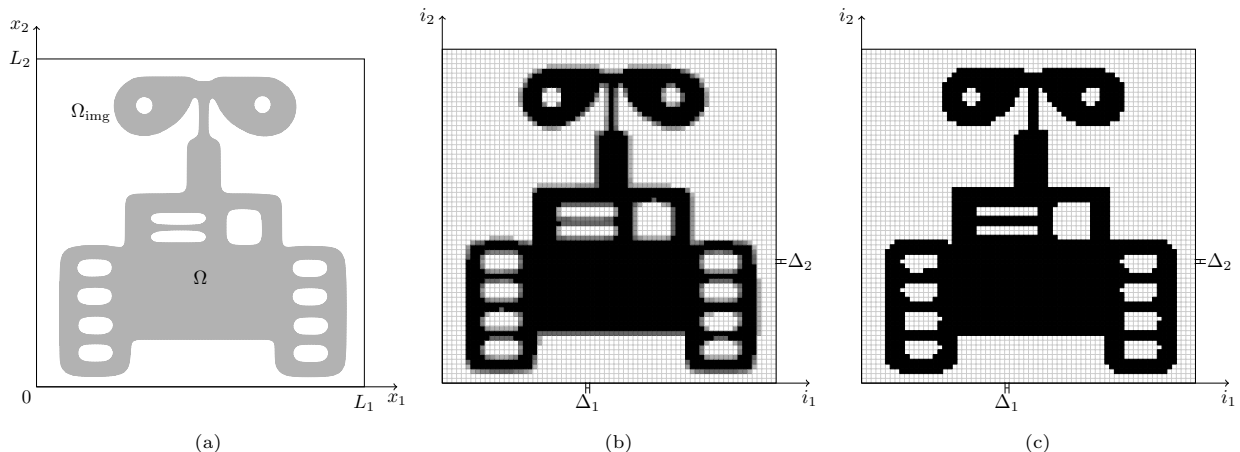


Figure 1: Representative two-dimensional geometry to illustrate the spline-based segmentation procedure. (a) The assumed geometry, which in a real-life scan-based analysis setting is evidently not available. (b) The grayscale data on a 75×75 voxel grid, which we derived from the exact geometry by computing the volume fraction of each voxel. In the scan-based analysis setting this voxel image is obtained directly from the scan data. (c) The segmented geometry for a grayscale threshold corresponding to 50% of the volume fraction.

2. Spline-based image segmentation

In this section we review the spline-based image segmentation procedure of Ref. [19]. The occurrence of topological anomalies on relatively coarse voxel grids is illustrated and explained using a Fourier analysis. Based on this analysis, a solution strategy to avoid topological anomalies is proposed.

2.1. B-spline level set construction

Consider an n_d -dimensional image domain, $\Omega_{\text{img}} = [0, L_1] \times \dots \times [0, L_{n_d}]$, which is partitioned by a set of voxels, as illustrated in Figure 1. We denote the voxel mesh by

$$\mathcal{V}_{\text{vox}} = \{\Omega_{\text{vox}} \subset \Omega_{\text{img}} \mid \exists \mathbf{i} \in \mathbb{Z}_{\geq 0}^{n_d}, \text{ s.t. } \Omega_{\text{vox}} = T_{\mathbf{i}} \circ [0, 1]^{n_d}\}, \quad (1)$$

where the transformation $T_{\mathbf{i}} : [0, 1]^{n_d} \rightarrow \Omega_{\text{vox}}$ is defined as

$$T_{\mathbf{i}}(\boldsymbol{\xi}) = \text{diag}(\boldsymbol{\Delta})(\boldsymbol{\xi} + \mathbf{i}), \quad (2)$$

with $\boldsymbol{\Delta}$ the voxel size in each direction and $\mathbf{i} = (i_1, \dots, i_{n_d})$ the n_d -dimensional voxel index. We denote the number of voxels in the voxel image by $m_{\text{vox}} = \#\mathcal{V}_{\text{vox}}$. The grayscale intensity function, illustrated in Figure 1b, is then defined as

$$g : \mathcal{V}_{\text{vox}} \rightarrow \mathcal{G}, \quad (3)$$

with \mathcal{G} the range of the grayscale data (e.g., from 0 to 255 for 8 bit unsigned integers). An approximation of the object Ω can be obtained by thresholding the gray scale data,

$$\Omega \approx \{\mathbf{x} \in \Omega_{\text{img}} \mid g(\mathbf{x}) > g_{\text{crit}}\} \subset \Omega_{\text{img}}, \quad (4)$$

where g_{crit} is the threshold value (see Figure 1c). As a consequence of the piecewise definition of the grayscale data in equation (3), the boundary of the segmented object is non-smooth when the grayscale data is segmented directly. In the context of analysis, the non-smoothness of the boundary can be problematic, as irregularities in the surface may lead to non-physical singularities in the solution to the problem.

The B-spline segmentation procedure in Ref. [19] – the behavior of which in the case of linear basis functions closely corresponds with that of marching volume algorithms [8] – enables the construction of a smooth boundary approximation based on voxel data. The key idea of this B-spline segmentation technique

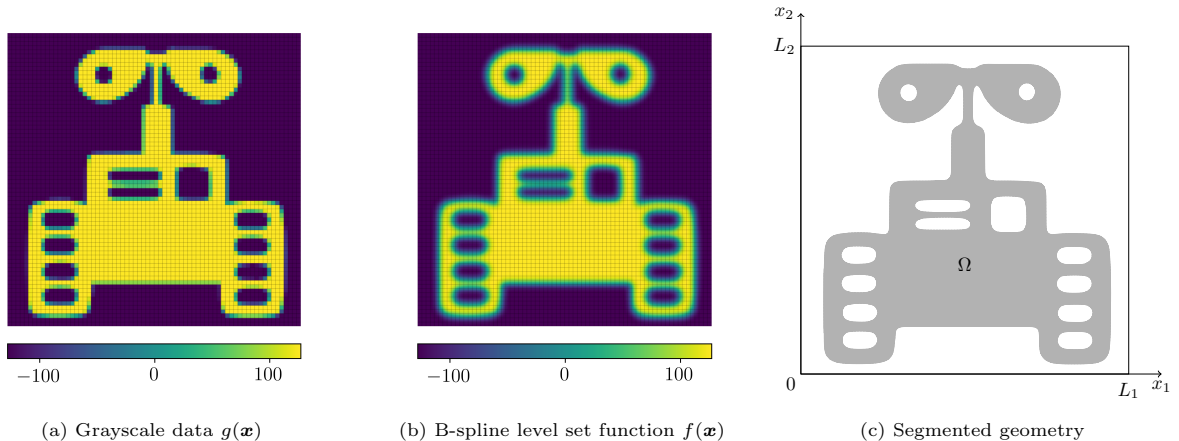


Figure 2: Illustration of the B-spline based segmentation procedure on a 70×70 voxel grid using second-order B-splines constructed on a regular mesh that coincides with the voxels. (a) Grayscale data, $g(\mathbf{x})$, of Figure 1b shown on the 8 bit signed integer range. (b) Level set function, $f(\mathbf{x})$, computed by equation (5). (c) Segmented domain extracted using the midpoint tessellation procedure outlined in Refs. [19, 45].

is to smoothen the grayscale function (3) by convoluting it using a B-spline basis of size n , $\{N_{i,k}(\mathcal{V}^h)\}_{i=1}^n$, defined over a regular mesh, \mathcal{V}^h , with fixed element size, h_d , per direction. Note that this mesh size can be different from the voxel size. The B-spline basis can be constructed using the Cox-de Boor algorithm [98]. We consider full-regularity (C^{k-1} -continuous) B-splines of order k , with the order assumed to be constant and isotropic. By convoluting the grayscale function (3), a smooth level set approximation is obtained as

$$f(\mathbf{x}) = \sum_{i=1}^n N_{i,k}(\mathbf{x})a_i, \quad a_i = \frac{\int_{\Omega_{\text{img}}} N_{i,k}(\mathbf{x})g(\mathbf{x})d\mathbf{x}}{\int_{\Omega_{\text{img}}} N_{i,k}(\mathbf{x})d\mathbf{x}}, \quad (5)$$

where the coefficients $\{a_i\}_{i=1}^n$ are the control point level set values.

The B-spline level set function corresponding to the voxel data in Figure 1b is illustrated in Figure 2 for the case where the regular mesh, \mathcal{V}^h , coincides with the voxel grid (*i.e.*, $\Delta_d = h_d$ for $d = 1, \dots, n_d$) and second order ($k = 2$) B-splines. As can be seen, the object retrieved from the convoluted level set function more closely resembles the original geometry in Figure 1a compared to the voxel segmentation in Figure 1c. Also, the boundaries of the domain are smooth as a consequence of the higher-order continuity of the B-spline basis (see Figure 2c). The segmented geometry in Figure 2c is constructed using the midpoint tessellation procedure proposed in Refs. [19, 45], which constructs a partitioning of the elements that intersect the domain boundary and results in an accurate parametrization of the interior volume. The reader is referred to Ref. [19] for a detailed discussion of the properties of the employed B-spline segmentation technique, and, additionally, to Ref. [45] for details regarding the midpoint tessellation procedure.

2.2. The occurrence of topological anomalies

The spline-based segmentation technique reviewed above has been demonstrated to yield computational domains that are very well suited for isogeometric analysis (see, *e.g.*, [36, 58, 72]). However, although the smoothing characteristic of the technique is frequently beneficial, it may lead to the occurrence of topological anomalies when the features of the object to be described are not significantly larger in size than the voxels (*i.e.*, the Nyquist criterion is not satisfied [19]).

For the object in Figure 1a this occurs when a voxel grid of 35×35 is considered, as illustrated in Figure 3 for a second-order ($k = 2$) B-spline basis defined on the 35×35 voxels mesh. As can be seen, small and slender features, such as the regions highlighted in green in Figure 3c, are detectable in the original grayscale data, albeit with a very coarse representation. The corresponding level set function is smoother, but introduces topological anomalies in the form of the disappearance of some of the small and slender

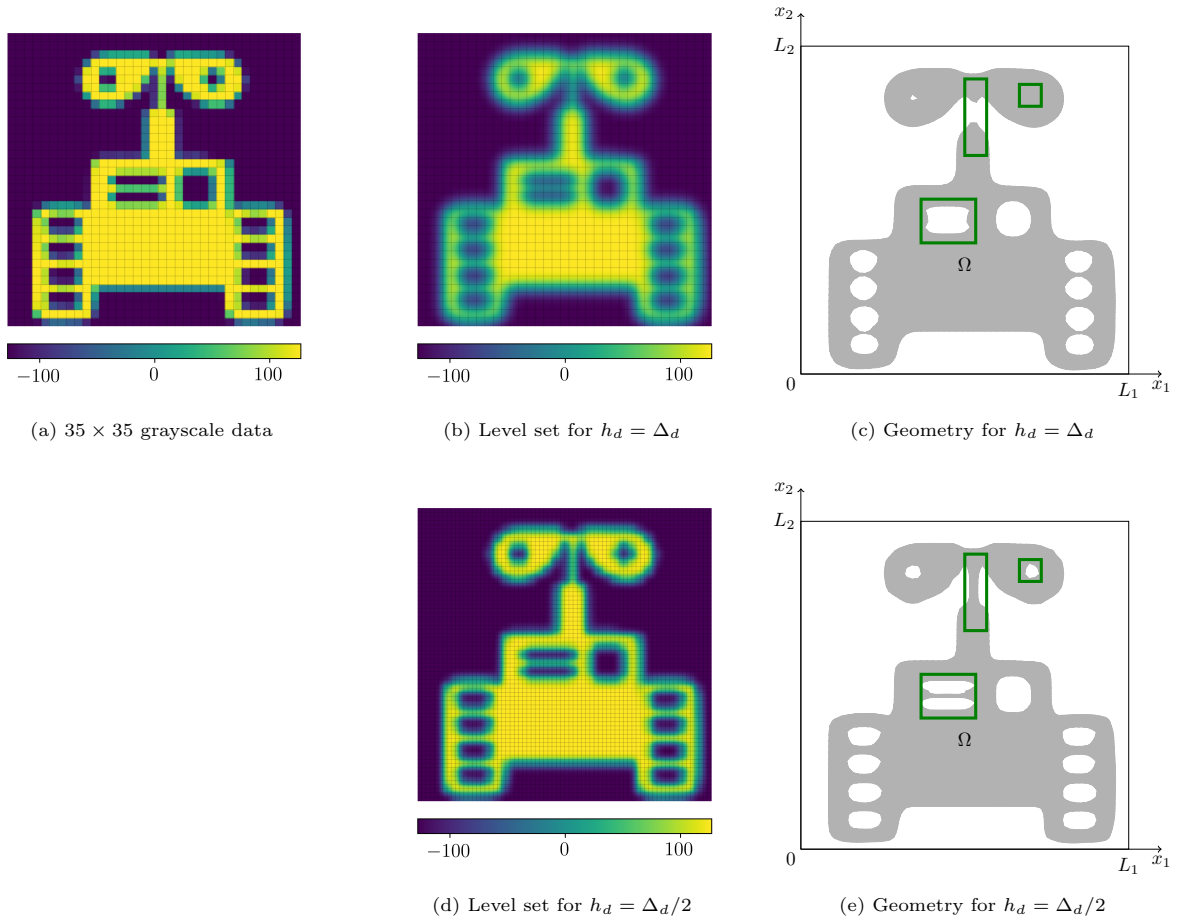


Figure 3: Illustration of the B-spline-based segmentation procedure for 35×35 voxel grayscale data (panel a). Using second-order B-splines constructed on a regular mesh that coincides with the voxels (panel b) leads to topological changes in the segmented domain (panel c) compared to the 70×70 voxels case in Figure 2. When the B-spline basis is constructed on a mesh that is twice as fine as the voxel grid, a smooth level set function is obtained (panel d) which, after segmentation, correctly represents the topology of the object (panel e).

features. When we consider the same voxel data, but now define the B-spline basis for the convolution of the level set function on a twice as fine mesh (see Figure 3d), *i.e.*, $h_d = \Delta_d/2$ for $d = 1, \dots, n_d$, a topologically correct segmented domain is again obtained, but still with smoothed boundaries (see Figure 3e) compared to the direct segmentation.

To elucidate the smoothing behavior of the B-spline segmentation technique, we generalize the filtering analysis for a univariate B-spline ($n_d = 1$) presented in Ref. [19] to the case of non-coinciding voxel and B-spline grid sizes, *i.e.*, $h \neq \Delta$. Note that, in the univariate setting considered here, we drop the index for the geometric direction to simplify our notation. The goal of our analysis is to provide insight into the filtering properties by considering the level set approximation in the frequency domain. Additionally, we will obtain an analytical expression for the smoothed level set function in the spatial domain with a parametrization that provides insight into the smoothing properties of the level set construction.

We commence our analysis with rewriting the operation (5) as an integral transform

$$f(x) = \int_{\Omega_{\text{img}}} \mathcal{K}(x, y) g(y) dy, \quad \mathcal{K}(x, y) = \sum_{i=1}^n \frac{N_{i,k}(x) N_{i,k}(y)}{V_i}, \quad (6)$$

where $\mathcal{K}(x, y)$ is the kernel of the transformation and where $V_i = \int_{\Omega_{\text{img}}} N_{i,k}(x) dx$ is the integral of the

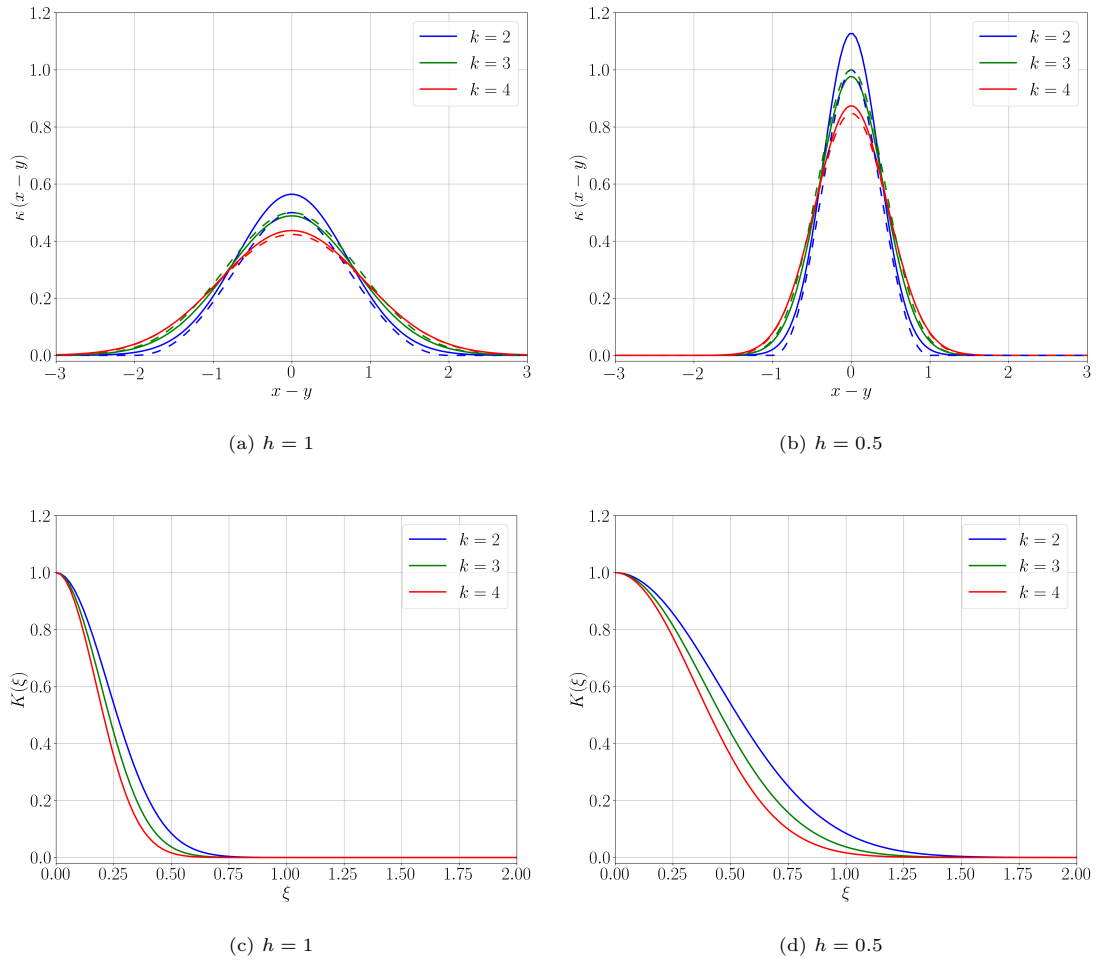


Figure 4: The convolution kernel (7) in the spatial domain (panels (a) and (b)), and in the frequency domain (panels (c) and (d)) for $k = 2, 3, 4$ using different mesh sizes. The integration kernel (6) is plotted in the spatial domain for reference (dashed lines).

basis function $N_{i,k}$. Following the derivation in Ref. [19] – in which the essential step is to approximate the B-spline basis functions by rescaled Gaussians [99] – the integration kernel (6) can be approximated by

$$\mathcal{K}(x, y) \approx \kappa(x - y) = \frac{1}{\sigma\sqrt{2\pi}} \exp\left(-\frac{(x - y)^2}{2\sigma^2}\right), \quad (7)$$

where the width of the smoothing kernel is given by

$$\sigma = h\sqrt{\frac{k+1}{6}}. \quad (8)$$

This result is very similar to that obtained in Ref. [19], with the important difference that the width of the kernel depends on the mesh size, h , on which the B-spline is defined, and not on the voxel size, Δ . Note that the approximate kernel κ depends on the difference between the coordinates x and y only, this in contrast to the kernel \mathcal{K} . Consequently, when the approximate kernel κ is considered, the integral transform (6) becomes a convolution operation.

The dependence of the convolution kernel on the mesh size and on the order of the B-spline interpolation is illustrated in Figures 4a and 4b. The B-spline integral transform around $x = 0$ computed on a domain of size 10 with a voxel size 1 is shown for reference, indicating that the Gaussian approximation improves with an increasing B-spline order. Figure 4 conveys that, following equation (8), increasing the mesh size and the B-spline order both increase the zone over which the grayscale data is averaged. The smoothing width scales linearly with the mesh size, and, for sufficiently large B-spline orders, with the square root of k .

To provide detailed insights into how the filter properties lead to topological anomalies, we express the convolution operation (6) with the approximate kernel (7) in the frequency domain as

$$F(\xi) = K(\xi)G(\xi), \quad (9)$$

where $F(\xi)$ and $G(\xi)$ are the Fourier transforms of the original grayscale data and the convoluted level set function, respectively, and where the Fourier transform of the convolution kernel (7) is given by

$$K(\xi) = \exp(-2\pi^2\xi^2\sigma^2). \quad (10)$$

This frequency-domain form of the kernel is shown in Figures 4c and 4d. The Fourier-form of the convolution operation in equation (9) conveys that features corresponding to frequencies for which $K(\xi)$ is close to unity are preserved in the smoothing operations, whereas features corresponding to frequencies for which $0 < K(\xi) \ll 1$ are filtered.

To further clarify the preservation of features, we consider a one-dimensional object of size ℓ , represented by the grayscale function (in both the spatial and in the frequency domain)

$$g(x) = \begin{cases} 1 & |x| < \ell/2 \\ 0 & \text{otherwise} \end{cases}, \quad G(\xi) = \ell \operatorname{sinc}(\ell\xi) = \frac{\sin(\pi\ell\xi)}{\pi\xi}. \quad (11)$$

The smooth approximation of this feature in the frequency domain follows from equation (9) as

$$F(\omega) = \ell \operatorname{sinc}(\ell\xi) \exp(-2\pi^2\xi^2\sigma^2). \quad (12)$$

The corresponding function in the spatial domain can be determined by expressing the sinc function as [100]

$$\operatorname{sinc}(\ell\xi) = \lim_{m \rightarrow \infty} \frac{1}{m} \sum_{n=1}^m \cos(2\mu(m, n)\pi\xi), \quad (13)$$

with $\mu(m, n) = \frac{(2n-1)\ell}{4m}$, such that the final form of the approximated convolution operation (6) can be written as

$$f(x) = \frac{\ell}{\sigma\sqrt{2\pi}} \lim_{m \rightarrow \infty} \frac{1}{2m} \sum_{n=1}^m \left[\exp\left(-\frac{(x - \mu(m, n))^2}{2\sigma^2}\right) + \exp\left(-\frac{(x + \mu(m, n))^2}{2\sigma^2}\right) \right]. \quad (14)$$

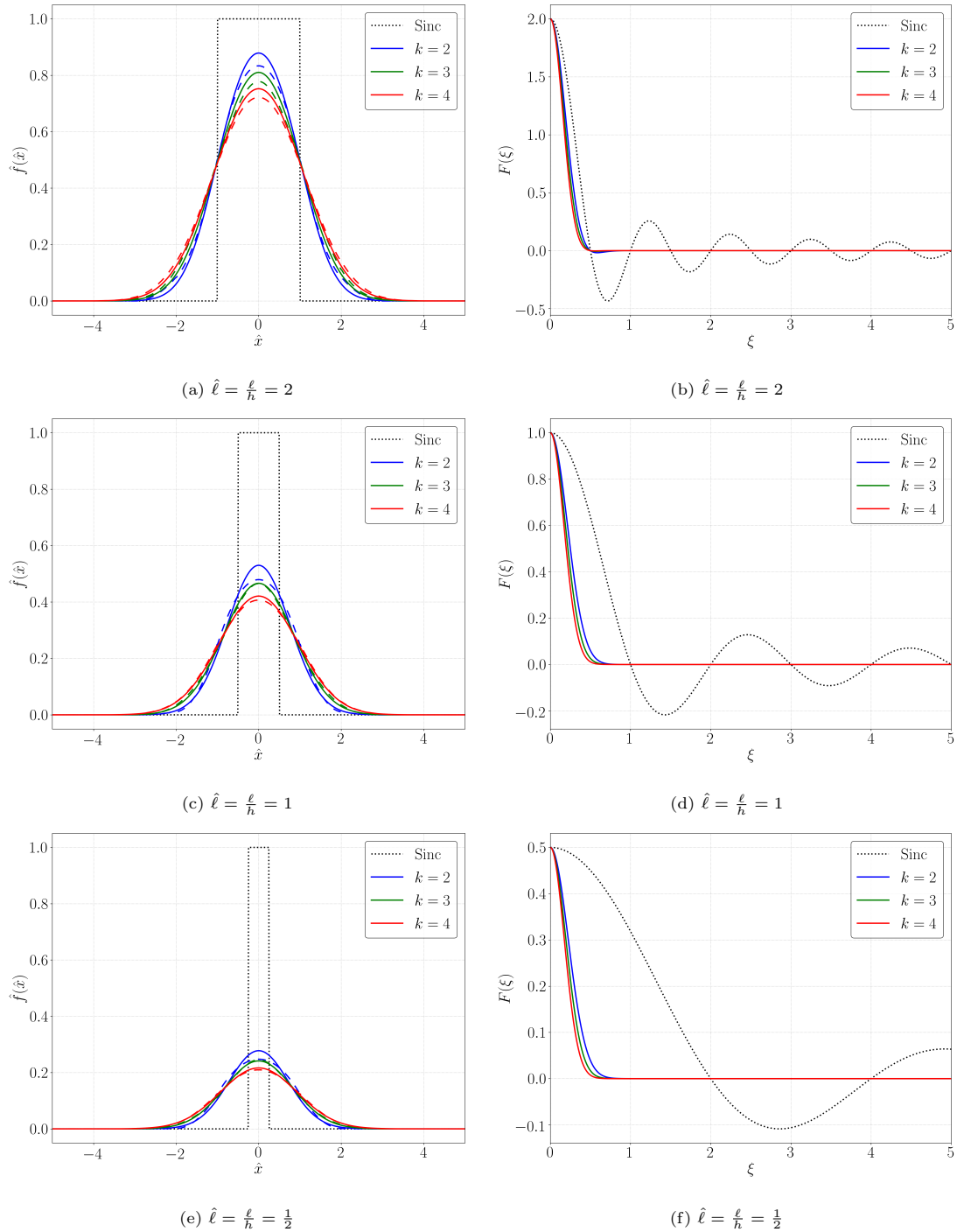


Figure 5: Smoothed level set approximation (14) of a geometric feature in the spatial domain (left) and in the frequency domain (right) for various feature-size-to-mesh ratios, $\hat{\ell} = \ell/h$, and B-spline degrees. The B-spline level set function (6) is shown in the spatial domain for reference (dashed lines).

The approximate level set function (14) is illustrated in Figure 5 for various feature-size-to-mesh ratios, $\hat{\ell} = \ell/h = 2, 1, \frac{1}{2}$, and B-spline degrees, $k = 2, 3, 4$. For the considered range of feature-size-to-mesh ratios, the limit in equation (14) is already approximated well with $m = 1$, such that

$$f(h\hat{x}) \approx \hat{f}_1(\hat{x}) = \sqrt{\frac{3\hat{\ell}^2}{4\pi(k+1)}} \left[\exp\left(-\frac{3(4\hat{x}-\hat{\ell})^2}{16(k+1)}\right) + \exp\left(-\frac{3(4\hat{x}+\hat{\ell})^2}{16(k+1)}\right) \right], \quad (15)$$

where $\hat{x} = x/h$. The value of the smoothed level set function at $\hat{x} = 0$ follows as

$$\hat{f}_1(0) = \sqrt{\frac{3\hat{\ell}^2}{\pi(k+1)}} \exp\left(-\frac{3\hat{\ell}^2}{16(k+1)}\right) \approx \hat{\ell} \sqrt{\frac{3}{\pi(k+1)}}, \quad (16)$$

which conveys that the maximum value of the smoothed level set depends linearly on the relative feature size $\hat{\ell}$, and decreases with increasing B-spline order.

The top row in Figure 5 shows the case for which the considered feature is twice as large as the mesh size, *i.e.*, $\hat{\ell} = 2$. Figure 5a illustrates that the sharp boundaries of the original grayscale function are significantly smoothed, which is also apparent from the frequency domain plot in Figure 5b, which shows that the high frequency modes required to represent the sharp boundary are filtered out by the smoothing operation. In Figure 5a, the decrease in the maximum level set value as given by equation (16) is observed. When the level set function is segmented by a threshold of $g_{\text{crit}} = 0.5$, a geometric feature that closely resembles the original one is recovered.

The middle and bottom rows of Figure 5 illustrate cases where the feature width is not significantly larger than the mesh size. For the case where the feature size is equal to the size of the mesh, the maximum of the level set function drops significantly compared to the the case of $\hat{\ell} = 2$. When considering second-order B-splines, the maximum is still marginally above $g_{\text{crit}} = 0.5$. Although the recovered feature is considerably smaller than the original one, it is still detected in the segmentation procedure. When increasing the B-spline order, the maximum value of the level set drops below the segmentation threshold, however, indicating that the feature will no longer be detected. As a consequence, the B-spline segmentation procedure then induces a topological alteration. When decreasing the feature length further, as illustrated in the bottom row of Figure 5, topological changes are encountered at lower segmentation thresholds. For the case of $g_{\text{crit}} = 0.5$, also the quadratic B-splines would lead to a loss of the feature.

In summary, the above analysis shows that topological anomalies occur when the relative feature length scale, $\hat{\ell} = \ell/h$, becomes too small. The smallest features in a voxel data file are of the size of a single voxel, *i.e.*, $\ell = \Delta$. Hence, topological features are lost when the mesh size on which the B-spline level set is constructed is relatively large compared to the voxel size. For moderate B-spline orders, this practically means that for features with the size of a single voxel, the mesh of the B-spline level set should be a uniform refinement of the voxel mesh, such that the relative feature size $\hat{\ell}$ is sufficiently large. With this mesh refinement, the resulting level set function will still be C^{k-1} -continuous, but higher-frequent modes are present in the refined level set function. In places where the geometric features are sufficiently large, this is in principle not desirable. Ideally, one only should refine the B-spline level set function in places where this is needed to preserve the topology, *i.e.*, around small features. In the next section, we propose a fully-automated topology-preserving B-spline segmentation strategy that refines the B-spline level set function in such a manner that topological anomalies are avoided.

3. Topology-preserving image segmentation using THB-splines

In this section we present a topology-preserving B-spline-based image segmentation strategy relying on the technique proposed in Ref. [19]. The proposed strategy consists of two steps (schematically illustrated in Figure 6). In the first step, which we will discuss in detail in Section 3.1, a moving-window strategy is applied to locally compare the topology of the original voxel data and its smoothly segmented counterpart.

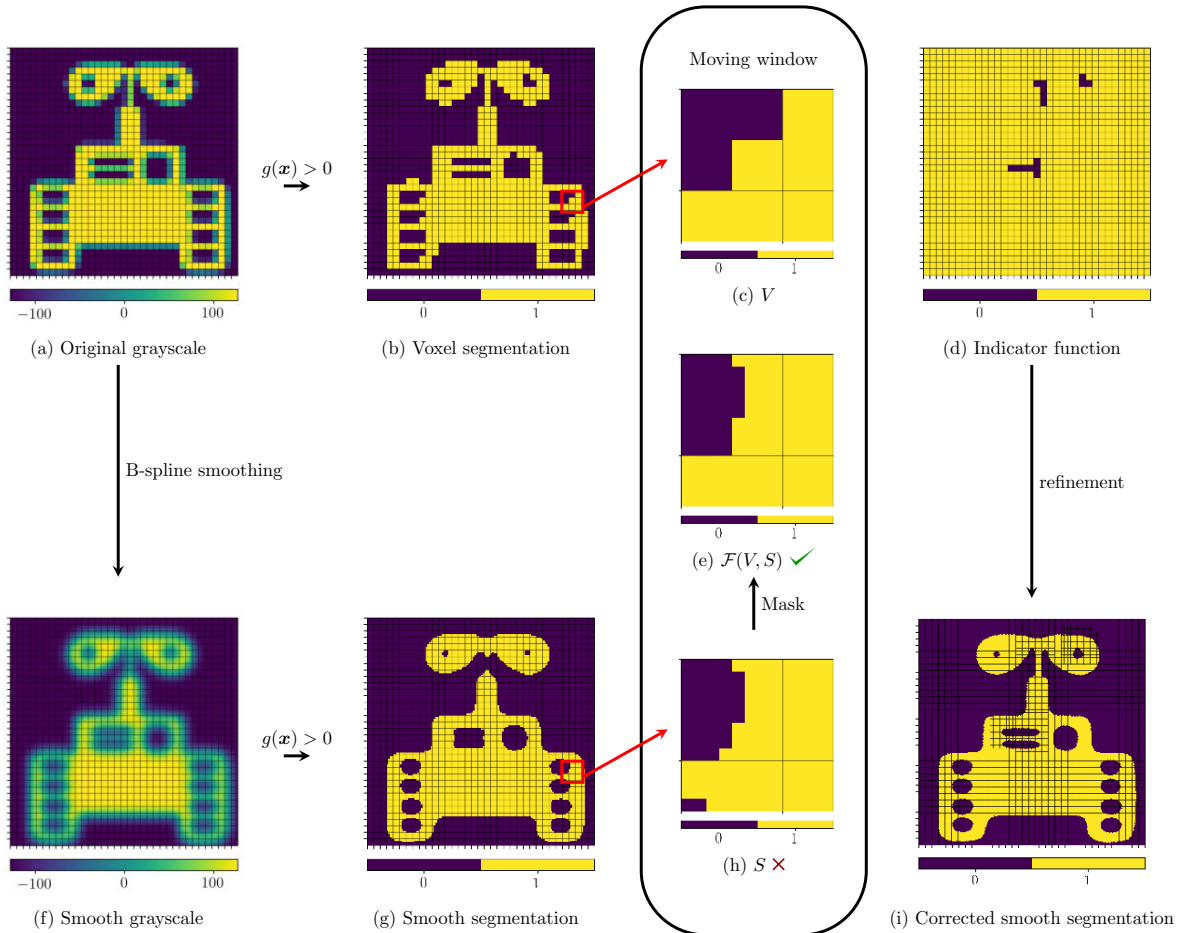


Figure 6: Illustration of the topology-preserving image segmentation procedure. The original grayscale image (panel a) is segmented in two ways, *viz.*, directly by thresholding the voxel data (panel b), and through the B-spline smoothing strategy (panels f and g). A moving-window technique then locally compares the topology between the two segmented images, which results in an indicator function (panel d) to mark topological differences. THB-spline-based refinements are then introduced to locally increase the resolution of the smooth level set function (panel i), thereby preserving the topology of the original image.

The result of this first step is a function that indicates regions where topological anomalies occur. In the second step, which is discussed in Section 3.2, truncated hierarchical (TH)B-splines are employed to locally repair the topology by mesh refinement, following the analysis presented in Section 2. To demonstrate the proposed image segmentation technique, various test cases, including the problematic scenario considered in Section 2, will be discussed in Section 3.3.

3.1. Moving-window topological anomaly detection

In this section we detail the moving-window strategy to detect topological anomalies. In Section 3.1.1 we commence with the definition of the moving window concept, as is commonly used in image processing techniques (*e.g.*, [101–103]). Subsequently, in Section 3.1.2 we introduce the window-comparison operator used to identify topological changes. A masking operation is finally introduced in Section 3.1.3 to distinguish between boundary changes and topological changes.

3.1.1. The moving window

To detect local topological changes, local views on the original voxel data and its smoothed counterpart will be compared. The windows are created by considering the r -neighborhood of each voxel in the original

image, *i.e.*,

$$\Omega_{\text{win}} = \mathcal{N}_r(\Omega_{\text{vox}}) \quad \forall \Omega_{\text{vox}} \in \mathcal{V}_{\text{vox}}. \quad (17)$$

The 0-neighborhood of a voxel is defined as the voxel itself, *i.e.*, $\mathcal{N}_0(\Omega_{\text{vox}}) := \Omega_{\text{vox}}$, and the r -neighborhood for $r \geq 1$ is defined recursively as the union of all voxels that share a vertex with the $(r - 1)$ -neighborhood. This window definition is illustrated in Figure 7 for a 10×10 voxel grid.

As discussed in Section 2, it is desirable to keep the mesh refinement to repair topological anomalies as local as possible. This means that the moving window should be as small as possible, but large enough to detect topological anomalies. Hence, the window should be larger than the size of the geometric features that are subject to topological changes. From the analysis in Section 2.2 it follows that features with a size similar to that of the voxels, *i.e.*, $\ell \approx \Delta$, can be subject to topological changes if the smoothing is performed on a mesh with a size similar to that of the voxels, *i.e.*, $h \approx \Delta$. Practically this means that a window with only a few rings, *i.e.*, $\ell \approx \Delta < (2r + 1)\Delta \ll L$, is expected to be an adequate choice. The influence of the window size will be studied for the example discussed in Section 3.3.

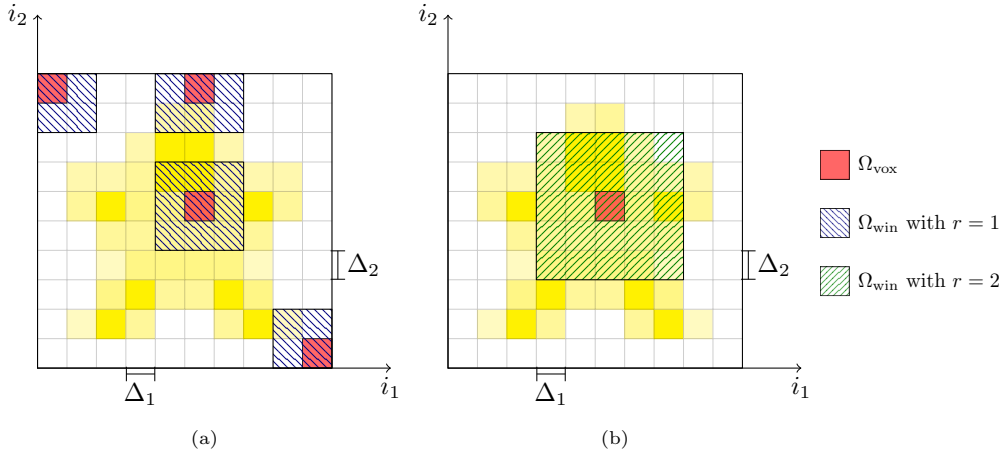


Figure 7: Illustration of the moving window Ω_{win} centered at a voxel Ω_{vox} , with (a) a one-neighborhood ($r = 1$) and (b) a two-neighborhood ($r = 2$).

3.1.2. Window image comparison

The moving-window technique indicates whether, for the window focused at every voxel, a topological difference is observed between the directly segmented image, V , and the geometry related to the smoothed image, S (see Figure 6). We herein employ the midpoint tessellation strategy proposed in Ref. [45] to construct a geometry parametrization, as illustrated in Figure 8a. Details of this procedure will be discussed in the context of the immersed isogeometric analysis framework discussed in Section 4. To enable the window topology comparison, it is convenient to employ the same representation concept for both images, V and S . Therefore, the tessellated geometry is first voxelized by segmentation of the B-spline level set function on a grid that is n_{sub} -times uniformly refined with respect to the original voxel grid, as shown in Figure 8b. This refinement level should be chosen such that the voxelization of the smoothed image does not induce topological changes compared to the geometry on which the simulation is performed. Since the employed midpoint tessellation strategy also relies on a recursive subdivision approach (of the computational cells), the number of voxel subdivisions, n_{sub} , can be related directly to the number of recursive refinements used for the midpoint tessellation (see Figure 8).

To characterize topological similarity, we define the window topology-comparison operator:

$$\mathcal{C}(V, S) = \begin{cases} \text{true} & \text{if } V \text{ and } S \text{ are topologically equivalent,} \\ \text{false} & \text{if } V \text{ and } S \text{ are topologically different.} \end{cases} \quad (18)$$

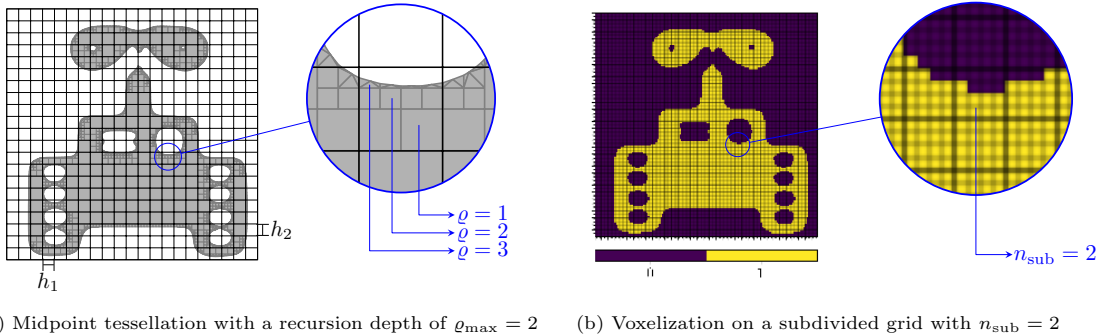


Figure 8: Schematic of (a) the midpoint tessellation procedure of Refs. [19, 45] and (b) the voxelization on a grid that is refined to match the recursion depth of the tessellation procedure.

To compute this boolean operator, the filled voxels in the images V and S are divided into connected regions. For the image V , for example, the regions are denoted by $R \in \mathcal{R}_V$, where \mathcal{R}_V is the set of all connected regions. We herein employ vertex-connectivity, meaning that voxels sharing a vertex are considered to be connected, but the same procedure can be applied using face-connectivity. For each connected region, R , we determine the Euler characteristic, $\chi(R)$, which is defined as one minus the number of connected holes, $\#\mathcal{V}_R$, in that region. Following the definition in Ref. [104], the Euler characteristic of the window image is given by

$$\chi(V) = \sum_{R \in \mathcal{R}_V} \chi(R) = \sum_{R \in \mathcal{R}_V} (1 - \#\mathcal{V}_R) = \#\mathcal{R}_V - \sum_{R \in \mathcal{R}_V} \#\mathcal{V}_R. \quad (19)$$

We note that various methods of evaluating the Euler characteristic have been rigorously studied in the field of homology, see, *e.g.*, Refs. [105–108]. In our work we consider the method of Ref. [104] which has been implemented in scikit-image [109], an open-source image processing library for Python.

To construct the boolean operator (18), we define sets of regions with a specific Euler characteristic, $\bar{\chi} \in \mathcal{X}_V = \{\chi(R) \mid R \in \mathcal{R}_V\} \subset \mathbb{Z}$, in an image as

$$\mathcal{R}_V^{\bar{\chi}} = \{R \in \mathcal{R}_V \mid \chi(R) = \bar{\chi}\}. \quad (20)$$

Figure 9 shows illustrative examples of these region sets. Using the region sets (20), the following indicator function for topological anomalies is proposed:

$$\mathcal{C}(V, S) = \left[\bigwedge_{\bar{\chi} \in \mathcal{X}_V \cup \mathcal{X}_S} (\#\mathcal{R}_V^{\bar{\chi}} \equiv \#\mathcal{R}_S^{\bar{\chi}}) \right] \bigwedge \left[\bigwedge_{\bar{\chi} \in \mathcal{X}_{V'} \cup \mathcal{X}_{S'}} (\#\mathcal{R}_{V'}^{\bar{\chi}} \equiv \#\mathcal{R}_{S'}^{\bar{\chi}}) \right] \quad (21)$$

This indicator states that the number of regions with a particular Euler characteristic is equal in the images V and S , as well as in their complements V' and S' . Note that, by construction, the operator (21) is invariant to the complement operation, *i.e.*, $\mathcal{C}(V, S) = \mathcal{C}(V', S')$, which makes the comparison operator objective with respect to the definition of the solid and void regions. One may note that if $\chi_V \neq \chi_S$ or $\chi_{V'} \neq \chi_{S'}$, then $\mathcal{C}(V, S)$ automatically reverts to false.

Figure 9 illustrates the comparison operator (21), where use has been made of a $n_{\text{sub}} = 3$ sampling of the B-spline-based segmented domain extracted using the midpoint tessellation procedure with $\varrho_{\text{max}} = 3$. The first row in Figure 9 shows a case where the topology matches, despite the substantial changes in geometry. The second row in Figure 9 shows a case where the elliptical region is missing, which is a typical case of a topological anomaly. The third row in Figure 9 shows a case in which the comparison operator returns false, which is caused by the appearance of a boundary spillover due to the smoothing procedure at the right bottom border. From the perspective of the window, the observed change indeed classifies as a topological change. However, when considering the change from the perspective of the complete image, the

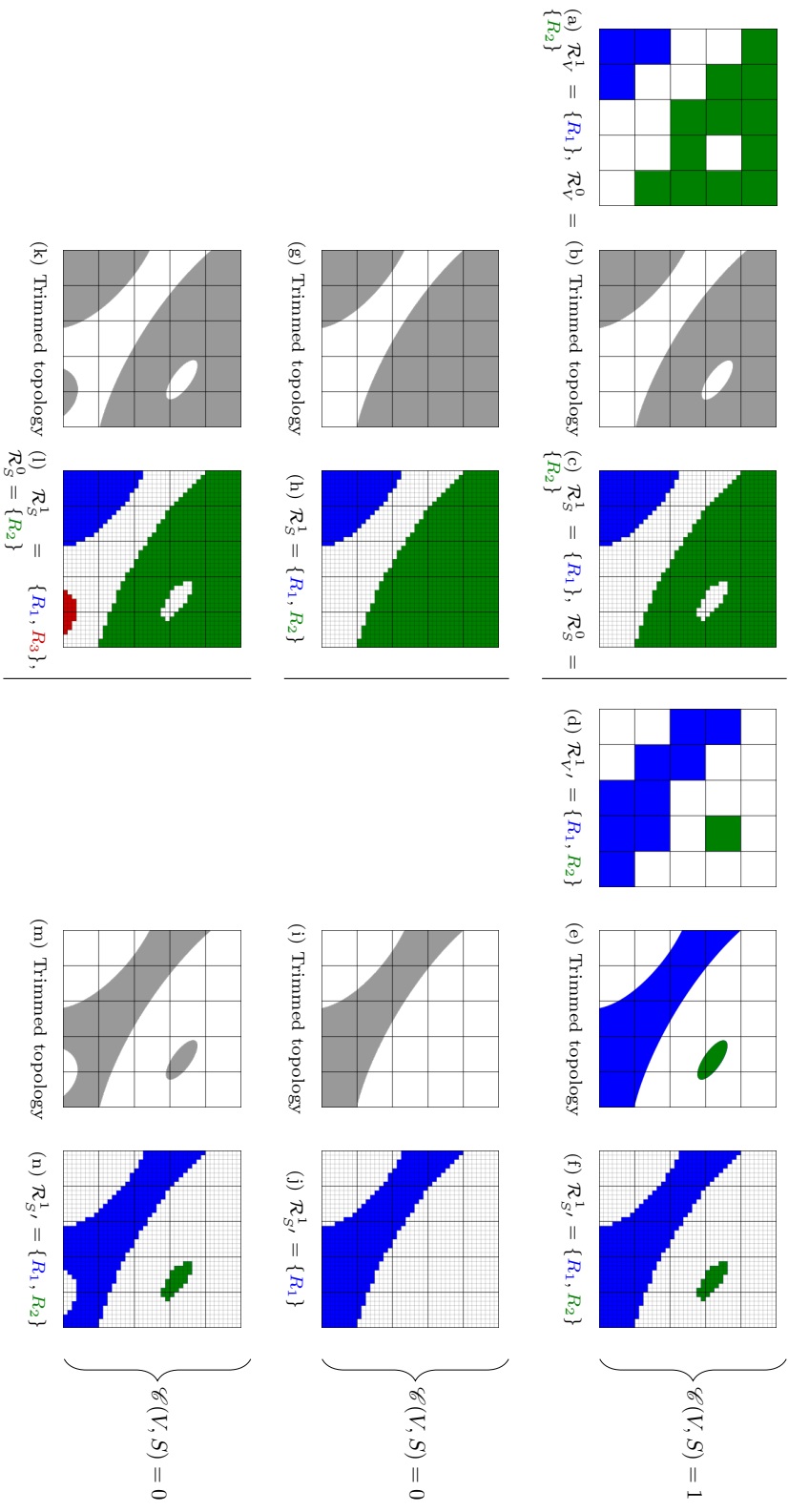


Figure 9: Illustration of the comparison operator (21) for the images V and V' (original gray scale data) in the first and fourth column and the image S and S' (B-spline-based segmented domain extracted using the midpoint tessellation procedure with $d_{\max} = 3$) in the second and fifth column. The third and sixth column are the $n_{\text{sub}} = 3$ voxelizations of the segmented domain. The images in the first row result in $\mathcal{C}(V, S) = \mathcal{C}(V', S') = 1$ as V and S are topologically equivalent. The images in the second row result in $\mathcal{C}(V, S) = \mathcal{C}(V', S') = 0$ as V and S are topologically different. The images in the third row result in $\mathcal{C}(V, S) = \mathcal{C}(V', S') = 0$ as V and S are topologically different due to a boundary spill over.

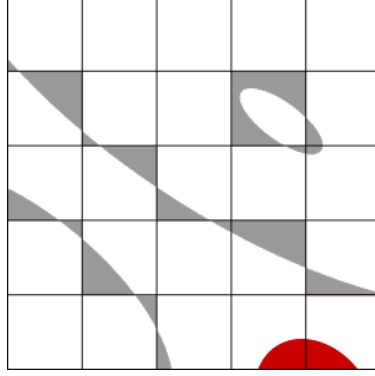


Figure 10: The symmetric difference (24) between the images V and S in Figure 9, with the boundary mask $M = \mathcal{M}(V, S)$ shown in red.

observed difference comes from a boundary that moves into the view of the window under consideration. This boundary movement classifies as a shape (geometry) change, and not as a topological change. To correctly account for this type of changes, in the next section we propose an image masking operation.

3.1.3. Window image masking

To mask the window changes associated with moving boundaries, as a preprocessing step to the comparison operation (21), the smoothed image S is masked using

$$F = \mathcal{F}(V, S) = (M \cap V) \cup (M' \cap S), \quad (22)$$

where F is the masked image and the mask M depends on arguments V and S , *i.e.*, $M = \mathcal{M}(V, S)$. This mask corresponds to a set-indication function which is one in places where a boundary change is detected and zero everywhere else. The mask is illustrated in Figure 10 for the case considered in the third row of Figure 9. The key idea behind this masking operation is that in regions where shape changes occur, the masked image F is replaced by the original voxel image V so that the changes associated with boundary movement are effectively reverted.

To identify the locations of the changes between the images V and S , we consider the mask to be a subset of the symmetric difference between the original and the smoothed image, *i.e.*, $M \subseteq V \Delta S = (V \cap S') \cup (S \cap V')$ (see Figure 10). We now only mask the regions in the symmetric difference which reside completely in the outer ring of the window *and* have an Euler characteristic of one (there are no voids), that is,

$$\mathcal{M}(V, S) = \{R \in \mathcal{R}_{V \Delta S}^1 \mid R \cap W_{r-1} = \emptyset\}, \quad (23)$$

where W_{r-1} is equal to zero in the outer voxel ring of the window and one everywhere else. Note that since the symmetric difference is unchanged when the complement images are considered, *i.e.*,

$$(V') \Delta (S') = (V' \cap S) \cup (S' \cap V) = V \Delta S, \quad (24)$$

for the mask (23) it holds that

$$\mathcal{M}(V', S') = \mathcal{M}(V, S) = M. \quad (25)$$

From this property of the mask it then follows that the complement of the masked image F is equal to the masked complement images V' and S' :

$$\begin{aligned} F' = \mathcal{F}(V, S)' &= (M \cap V)' \cap (M' \cap S)' = (M' \cup V') \cap (M \cup S') \\ &= [M' \cap (M \cup S')] \cup [V' \cap (M \cup S')] = (M' \cap S') \cup (V' \cap M) \cup (V' \cap S') \\ &= (M' \cap S') \cup (V' \cap M) \cup (V' \cap S' \cap M) \cup (V' \cap S' \cap M') = (M \cap V') \cup (M' \cap S') \\ &= \mathcal{F}(V', S') \end{aligned} \quad (26)$$

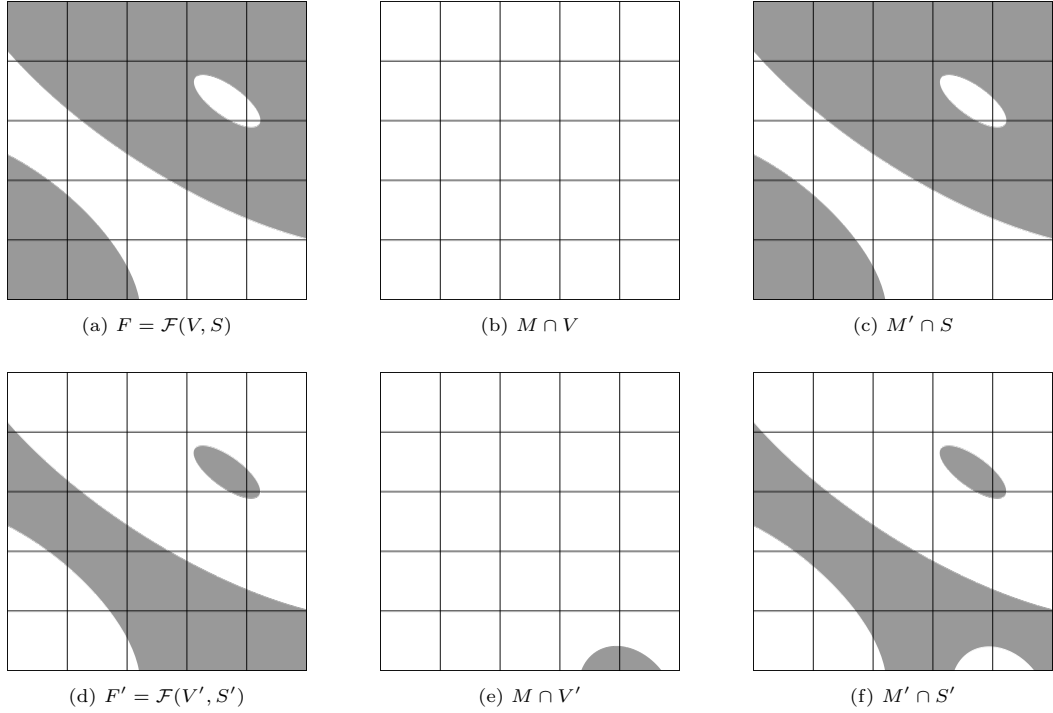


Figure 11: An illustration of the filtering operation (22) for an image V and the corresponding smoothed image S (see Figure 12) and for their complements.

The choice to identify shape changes associated with moving boundaries by definition (23) is motivated by the idea that if one considers a boundary in the global image with small curvature, the image smoothing operation discussed in Section 2 will typically retain the movement of the boundary within one voxel spacing. When the curvature of the boundary is locally high, the boundary movement can be larger than a single voxel, which would lead to falsely identifying a shape change as a topological change. In our algorithm this would lead to a refinement of the level set function which would not be strictly required to preserve topology. Avoiding such auxiliary refinements would, however, severely complicate the algorithm. Moreover, since they generally result in an improved geometry representation at high-curvature boundaries, it is considered desirable not to avoid them.

The masking operation (22) is illustrated in Figure 11 for an exemplifying image V and its smoothed version S (as defined in Figure 12), as well as for the complements of these images. The symmetric difference between the images V and S is shown in Figure 12c, which, in agreement with equation (24), is identical to the symmetric difference between V' and S' in Figure 12f. The masked regions are color coded in red, indicating that only completely solid regions in the outer ring are considered in the mask. The masked images $F = \mathcal{F}(V, S)$ and $F' = \mathcal{F}(V', S')$ are shown in Figures 11a and 11d, from which it is observed that, in accordance with equation (26), the complement of the masked image F is equal to the masked complement image $\mathcal{F}(V', S')$.

In Figure 13 we consider the case of the third row of Figure 9. As discussed above, when the images V and S are compared directly, the comparison operator (21) marks these images to be topologically different on account of the shape change associated with the boundary movement. When comparing the image V with the masked image $F = \mathcal{F}(V, S)$, as shown in Figure 13, the images are considered to be topologically equivalent, which, in this case, is considered as the correct indicator result.

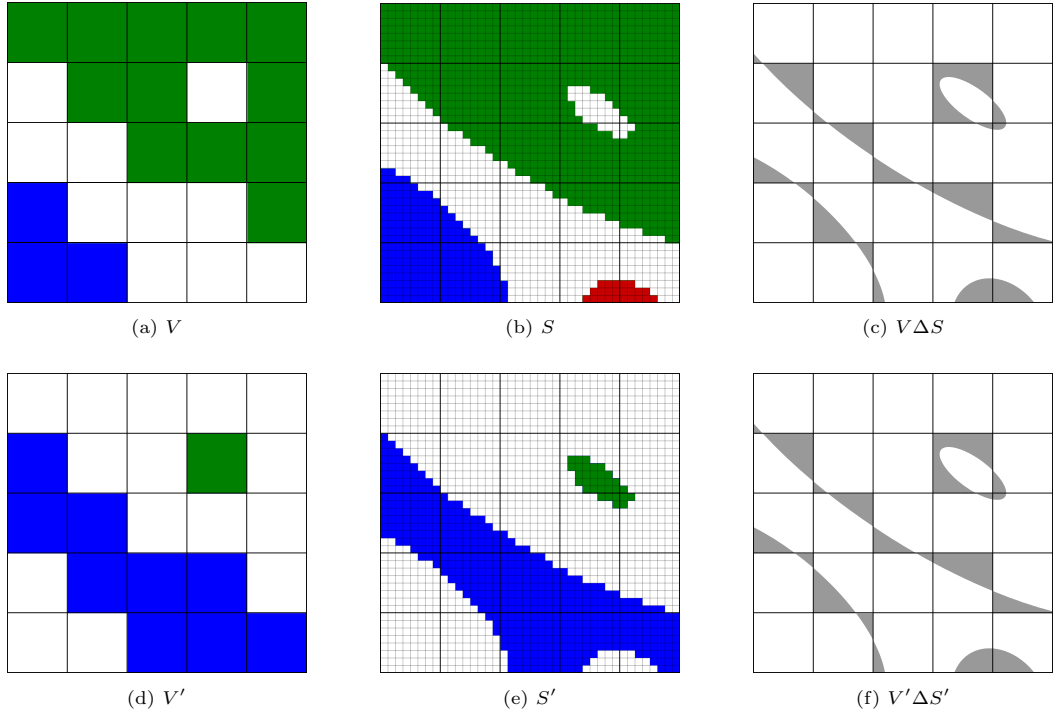


Figure 12: An example of (a) the original segmented image V , (b) the spline-based segmented image S , and (c) the symmetric difference. Panels (d) and (e) are the complements of V and S , respectively. Panel (f) is the symmetric difference of the complements, which is identical to that in panel (c).

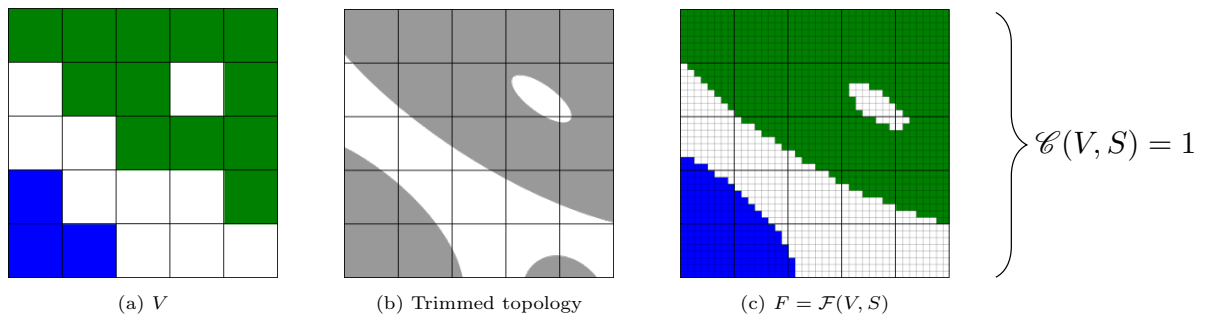


Figure 13: An illustration of the boundary masking procedure applied to the case in the third row of Figure 9. The image V in panel (a) is compared with the masked image F in panel (c) to obtain the indicator function $\mathcal{C}(V, S)$. In contrast to the result in Figure 9, the masking operation results in a $\mathcal{C}(V, S) = 1$, indicating that the images V and S are topologically equivalent.

3.2. THB-spline-based refinement strategy

After identification of the windows in which topological changes occur, the mesh on which the level set function is constructed is locally refined to resolve these anomalies (see Figure 6). More specifically, a support-based refinement procedure is employed, in which all basis functions that are supported on a voxel that displays a topological anomaly are replaced by basis functions from the next higher hierarchical level.

We herein employ truncated hierarchical B-splines [92–94] to construct a spline basis over locally refined meshes. The THB-spline construction is illustrated in Figure 14, which, for the sake of generality, considers the case of multiple refinement levels, with the level $\ell = 0$ corresponding to the coarsest elements, and the level $\ell = \ell_{\max}$ to the most refined elements. We denote the region covered by elements that are at least ℓ times refined by Ω^ℓ (note that the refinement regions are nested, *i.e.*, $\Omega^\ell \subseteq \Omega^{\ell-1} \subseteq \dots \subseteq \Omega^0 = \Omega_{\text{vox}}$). The locally refined mesh corresponding to these refinement regions is denoted by \mathcal{V}_{vox} .

To construct the truncated hierarchical B-spline basis, we consider ℓ_{\max} uniform refinements, $\mathcal{V}_{\text{vox}}^\ell$, of the original voxel mesh $\mathcal{V}_{\text{vox}}^0$. The mesh size of the original voxel mesh is denoted by h and that of its refinements by $2^{-\ell}h$. With each level we associate a mesh

$$\mathcal{V}^\ell = \{v \in \mathcal{V}_{\text{vox}}^\ell \mid v \cap \Omega^\ell \neq \emptyset\}. \quad (27)$$

We define a B-spline basis of degree k and regularity α over each of these meshes as

$$\mathcal{B}(\mathcal{V}^\ell) = \{N \in \mathcal{B}(\mathcal{V}_{\text{vox}}^\ell) \mid \text{supp}(N) \cap \Omega^\ell \neq \emptyset\}, \quad (28)$$

where $\mathcal{B}(\mathcal{V}_{\text{vox}}^\ell)$ is the B-spline basis on $\mathcal{V}_{\text{vox}}^\ell$.

To construct the truncated hierarchical B-spline basis, splines from the bases over the uniform meshes (28) are selected and truncated. On the most refined level, *i.e.*, at $\ell = \ell_{\max}$, all basis functions that are completely inside $\Omega_{\text{vox}}^{\ell_{\max}}$ are selected:

$$\mathcal{H}(\mathcal{V}^{\ell_{\max}}) = \{N \in \mathcal{B}(\mathcal{V}^{\ell_{\max}}) \mid \text{supp}(N) \subseteq \Omega^{\ell_{\max}}\}. \quad (29)$$

At coarser levels, *i.e.*, $0 \leq \ell < \ell_{\max}$, the functions that are completely inside the domain Ω^ℓ , but not completely inside the refined domain $\Omega^{\ell+1}$, are selected and truncated:

$$\mathcal{H}(\mathcal{V}^\ell) = \{\text{trunc}(N) \mid N \in \mathcal{B}(\mathcal{V}^\ell), \text{supp}(N) \subseteq \Omega^\ell, \text{supp}(N) \not\subseteq \Omega^{\ell+1}\} \quad (30)$$

The truncation operation reduces the support of the B-spline functions by projecting away basis functions retained from the refined levels (see Ref. [92, 110] for details). The THB-spline basis then follows as

$$\mathcal{H}(\mathcal{V}) = \bigcup_{\ell=0}^{\ell_{\max}} \mathcal{H}(\mathcal{V}^\ell). \quad (31)$$

This selection and truncation procedure is illustrated in Figure 14. It is noted that THB-splines satisfy the partition of unity property (in contrast to non-truncated hierarchical B-splines), which is an important property from the perspective of the image smoothing procedure (5) as it guarantees that the average grayscale intensity is preserved [19]. In this work we employ the THB-spline implementation in the Python-based open source numerical library Nutils [111], which is based on the element-wise construction discussed in Ref. [112].

3.3. Examples

To illustrate the topology preserving segmentation strategy presented above we consider the example presented in the workflow in Figure 6. The voxelized smooth image with $n_{\text{sub}} = 2$ is shown in Figure 6g, which closely resembles the tessellated image with a bi-sectioning depth of $\varrho_{\max} = 3$ in Figure 3c. By comparison with the voxel segmentation in Figure 6b, it is clearly observed that topological changes occur at two locations. These locations are highlighted in green in Figure 15c.

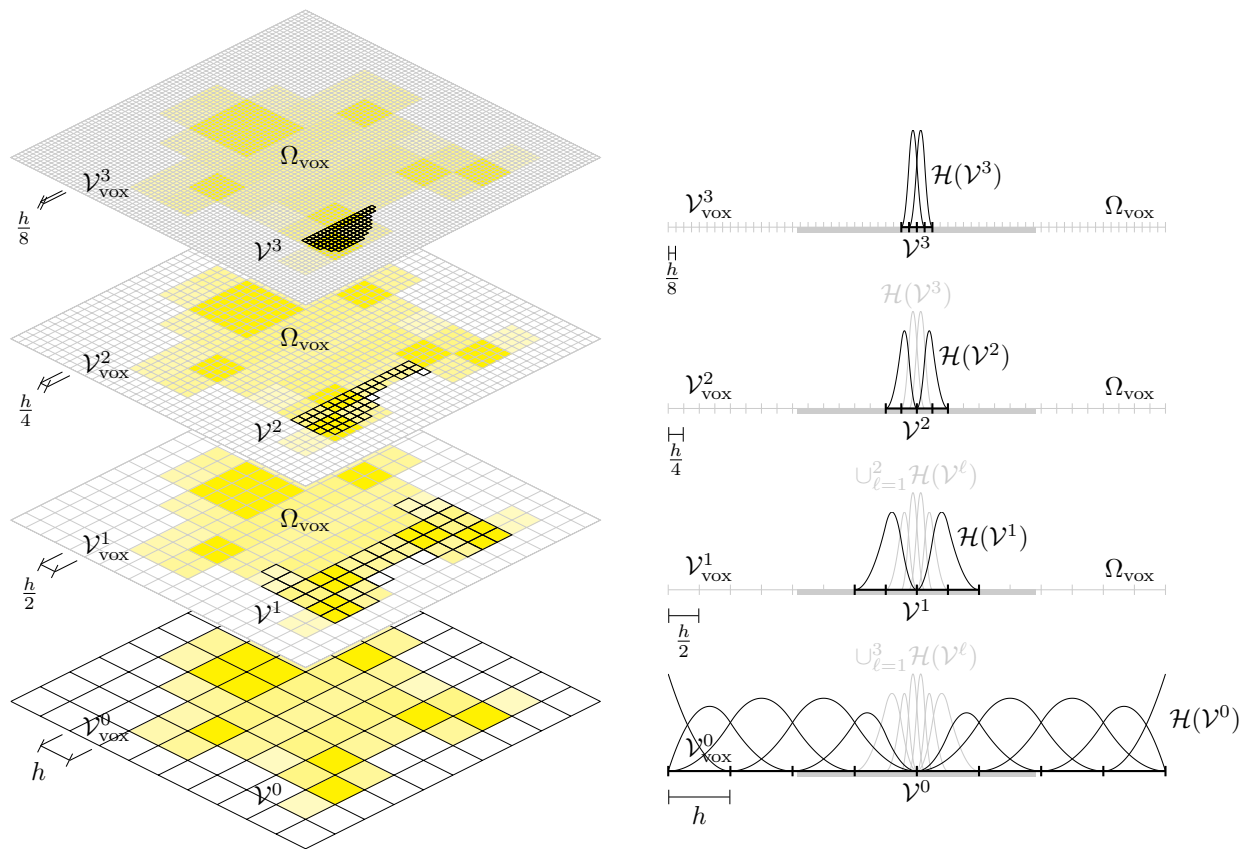


Figure 14: An illustration of truncated hierarchical B-splines. The left column shows the hierarchical levels of a mesh \mathcal{V}_{vox} , while the right column illustrates the concept for a one-dimensional voxel domain Ω_{vox} .

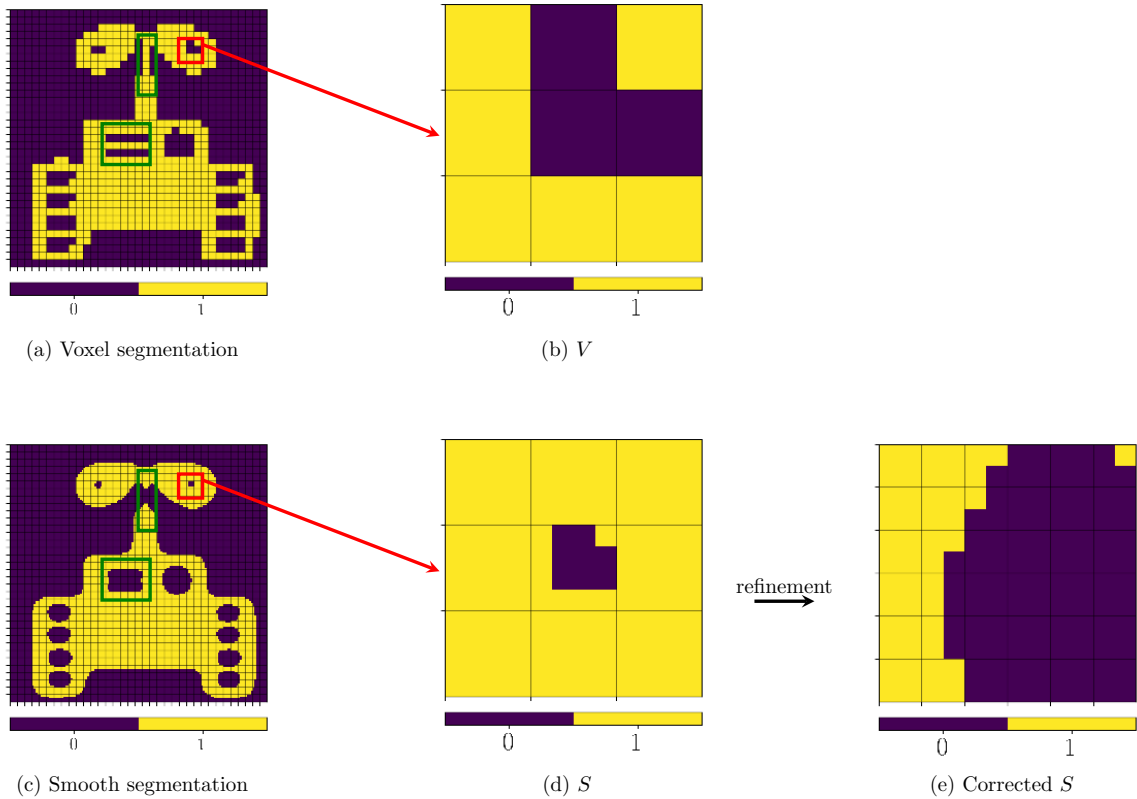


Figure 15: Example of the moving window strategy with a 3×3 window. Topological changes are correctly detected in the green boxes. In the red window, an L-shaped exclusion which extends beyond the outer ring of the window is falsely detected as a topological change.

Figure 6d presents the comparison indicator for a window size of 3×3 ($r = 1$). It is observed that the topological changes are indeed detected. Note that for this example, the mask operation is also active. As an example of the mask operation, Figure 6h shows a region with a boundary change before the mask operation. It is observed that the indicator function for topological anomalies (21) results in zero (false) when compared to the voxel region in Figure 6c. Figure 6e shows the region after the mask operation. After application of the mask, the comparison operator results in one (true).

In Figure 6d it is seen that an additional region, highlighted in red in Figure 15c, is also marked as a topological change. Strictly speaking, this would not be necessary, as in both images a hole is present in that region. Figure 15b shows the window causing this behavior. In the voxel image, the L-shaped exclusion is not detected as a hole in a region, but as a void region splitting two solid regions. On the level of the window, this is a topologically ambiguous case in the sense that one needs to look outside of the window to see whether the exclusion extends beyond the window. As shown in Figure 6i and in the zoom in Figure 15e, the effect of refining the level set in this region is that the voxel geometry is better captured.

In Figure 16 the influence of the window size is examined. As can be seen, the refinement regions increase in size with increasing window size. Since the 3×3 window already adequately corrects the topological anomalies, the growth of the refinement regions is unnecessary. As can be seen, the effect of a larger window size on the corrected images is minimal, as elaborated in Section 2.2. In Figure 16b and 16c we also observe a case where a shape change is marked as a topological change, which, as discussed in Section 3.1.3, is caused by the high curvature of the boundary. A zoom of a typical window in which this occurs is shown in Figure 17. It is also observed in Figure 16c that for the incorrectly identified topology change discussed

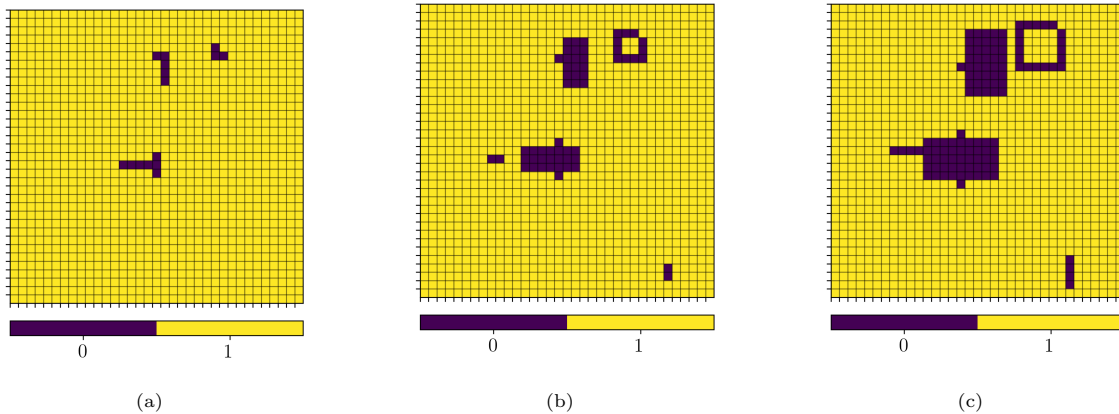


Figure 16: The comparison indicator function for the case considered in Figure 6 with a window size of (a) 3×3 ($r = 1$), (b) 5×5 ($r = 2$), and (c) 7×7 ($r = 3$).

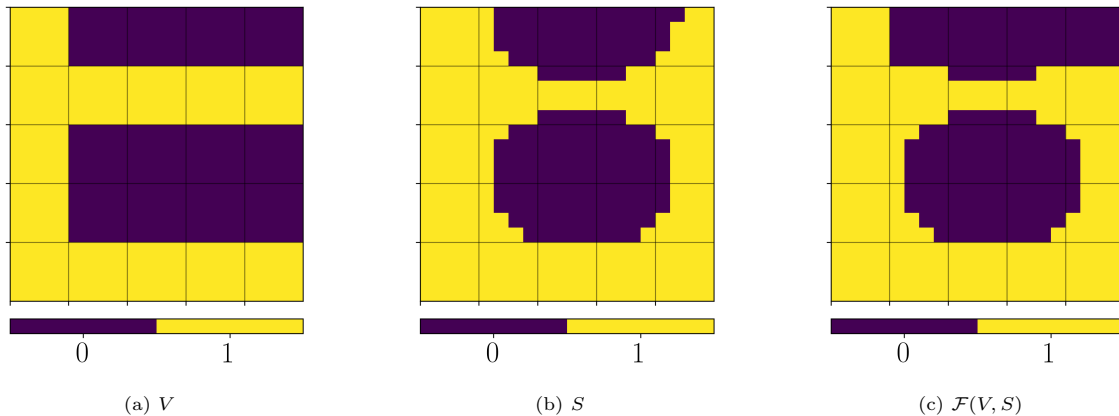


Figure 17: A 5×5 window showing an example of a shape change associated with a high curvature region. Since this shape change extends beyond the outer ring of the window, it is not masked and hence it is (incorrectly) detected as a topological change.

above, increasing the window size results in an indicator function in the form of a ring. This situation is not further explored in this work, but would require tailoring of the refinement marking strategy to ensure that the interior of the ring is refined.

4. The isogeometric finite cell method

To provide a basis for the boundary value problems considered in Section 5, in this section the abstract formulation for the isogeometric finite cell method [61] is introduced. We consider a physical domain, Ω , formed by the topology-preserving segmentation procedure outlined above. The domain and its boundary, $\partial\Omega$, are immersed into an ambient domain $\mathcal{A} \supset \Omega$ as shown in Figure 18. In the remainder we consider the ambient domain to coincide with the image (scan) domain, *i.e.*, $\mathcal{A} = \Omega_{\text{img}}$.

We suppose that the problem under consideration is described by a field variable u – which can be scalar-valued or vector-valued – and the weak formulation

$$\begin{cases} \text{Find } u \in W \text{ such that:} \\ a(u, v) = f(v) \quad \forall v \in V, \end{cases} \quad (32)$$

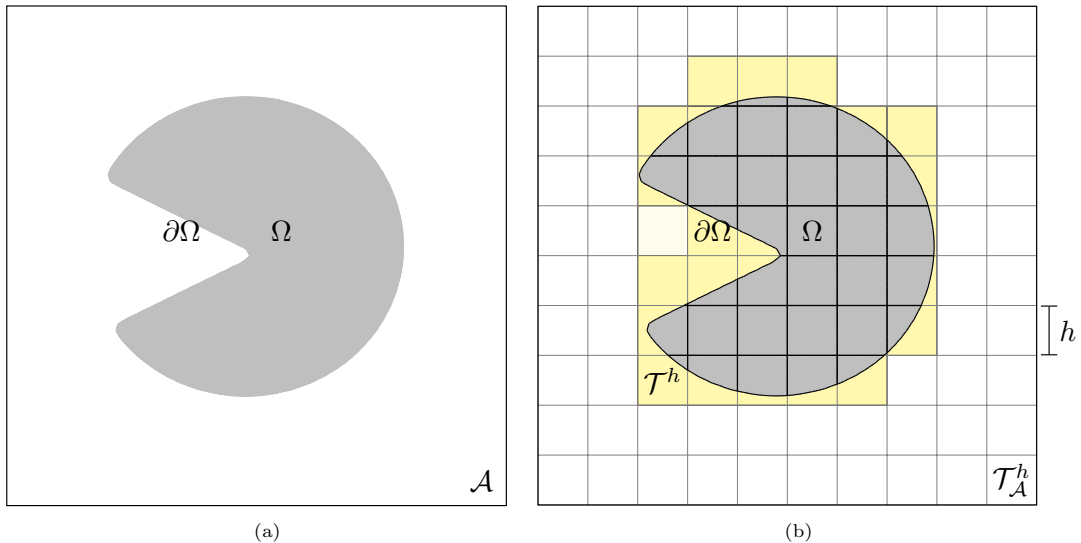


Figure 18: Schematic representation of (a) the physical domain Ω (gray) with boundary $\partial\Omega$ which is embedded in the ambient domain \mathcal{A} , and (b) the ambient domain mesh $\mathcal{T}_{\mathcal{A}}^h$ and the background mesh \mathcal{T}^h (yellow), with mesh size parameter h .

where W is the trial (solution) space, V is the test space, $a : W \times V \rightarrow \mathbb{R}$ is a continuous bilinear form and $b : V \rightarrow \mathbb{R}$ is a continuous linear form. The (isogeometric) finite cell method provides a general framework for constructing the finite dimensional subspaces $W^h \subset W$ and $V^h \subset V$, where the superscript h refers to the mesh parameter associated with the ambient domain mesh, $\mathcal{T}_{\mathcal{A}}^h$, on which the approximation to the field variable u is computed. Note that the mesh $\mathcal{T}_{\mathcal{A}}^h$ can be different from the level set mesh \mathcal{V}^h discussed in Section 2, as the mesh resolution requirements following from the approximation of the field variable u generally differ from those for the level set function.

We define the background mesh as all elements in the ambient domain that touch the physical domain, *i.e.*,

$$\mathcal{T}^h := \{K \in \mathcal{T}_{\mathcal{A}}^h : K \cap \Omega \neq \emptyset\}, \quad (33)$$

and the interior mesh of the domain Ω as

$$\mathcal{T}_{\Omega}^h := \{K \cap \Omega : K \in \mathcal{T}_{\mathcal{A}}^h\}, \quad (34)$$

where the elements in the background mesh are trimmed to the physical domain (see Ref. [45] for details). The physical domain boundary mesh is defined as

$$\mathcal{T}_{\partial\Omega}^h := \{K \cap \partial\Omega : K \in \mathcal{T}_{\mathcal{A}}^h\}. \quad (35)$$

The finite dimensional subspaces W^h and V^h are then constructed using THB-splines (as elaborated in Section 3.2). We denote the THB-spline space of degree k and regularity α , constructed over the locally-refined ambient domain $\mathcal{T}_{\mathcal{A}}^h$, by

$$S_{\alpha}^k(\mathcal{A}) = \{N \in C^{\alpha}(\mathcal{A}) : N|_K \in P^k(K), \forall K \in \mathcal{T}_{\mathcal{A}}^h\}, \quad (36)$$

where $P^k(K)$ is the collection of n_d -variate polynomials on the element $K \subset \mathbb{R}^{n_d}$. The approximation spaces are then obtained by restricting the THB-splines in $S_{\alpha}^k(\mathcal{A})$ to the physical domain Ω :

$$W^h = V^h = \{N|_{\Omega} : N \in S_{\alpha}^k(\mathcal{A})\}. \quad (37)$$

Due to the non-mesh-conforming character of the (isogeometric) finite cell method, it is infeasible to impose Dirichlet boundary conditions by (strongly) constraining functions in the spaces (37). Instead, Dirichlet

conditions are imposed weakly through Nitsche’s method [46, 48]. By employing a mesh-dependent consistent stabilization term, a well-posed Galerkin problem is obtained:

$$\begin{cases} \text{Find } u^h \in W^h \text{ such that:} \\ a^h(u^h, v^h) = b^h(v^h) \quad \forall v^h \in V^h \end{cases} \quad (38)$$

In this problem the bilinear form $a^h : W^h \times V^h \rightarrow \mathbb{R}$ and linear form $b^h : V^h \rightarrow \mathbb{R}$ are the finite dimensional versions of the operators in (32), augmented with the above-mentioned Nitsche terms (which will be specified in Section 5).

Although the Galerkin problem (38) closely resembles that of mesh-conforming finite element formulations, the immersed setting requires a dedicated consideration of various computational aspects. In the context of this work, the following aspects are particularly noteworthy:

Ghost-penalty and skeleton-penalty stabilization. To avoid ill-conditioning associated with small volume-fraction trimmed cells, we apply ghost-penalty stabilization [54]. The idea behind this stabilization technique is to penalize the jump in the (higher-order) normal gradients of the solution along all edges in the ghost mesh

$$\mathcal{F}_{\text{ghost}}^h = \{\partial K \cap \partial K' | K, K' \in \mathcal{T}^h, K \cap \partial\Omega \neq \emptyset, K \neq K'\}, \quad (39)$$

by augmenting the bilinear form with an additional ghost-penalty term. This ghost-penalty term, which will be detailed for the specific problems considered in Section 5, also enables scaling of the Nitsche penalty term by the reciprocal mesh size parameter of the background mesh (independent of the trimmed-element configurations) [50].

For the flow problems considered in this work, we employ equal-order discretizations. To make the considered mixed velocity/pressure-discretizations inf-sup stable, we apply skeleton-stabilization [36] to the pressure space along all edges in the skeleton mesh

$$\mathcal{F}_{\text{skeleton}}^h = \{\partial K \cap \partial K' | K, K' \in \mathcal{T}^h, K \neq K'\}. \quad (40)$$

The skeleton-penalty term with which the bilinear form is augmented will be specified in Section 5.

Numerical integration on trimmed elements. To evaluate integrals over the trimmed elements, we consider a recursive octree bisectioning strategy (see, *e.g.*, Ref. [19, 20]), with the maximum number of bisections equal to ϱ_{max} . On the lowest level of bisectioning, *i.e.*, $\varrho = \varrho_{\text{max}}$, the midpoint tessellation procedure detailed in Ref. [45] is employed to construct an explicit parametrization of the trimmed boundary. An illustration of the octree bisectioning procedure with the midpoint tessellation is shown in Figure 8a.

Considering equal-order (Gauss) integration schemes on all sub-cells in the tessellated trimmed elements leads to high computational costs, in particular when three-dimensional simulations are considered [45]. Various methods have been proposed to reduce the computational cost, *e.g.*, smart octree methods [43], moment fitting techniques [44], and error-estimate-based adaptive integration [45]. We herein consider the error-informed manual selection strategy proposed in Ref. [45]. At the coarsest level ($\varrho = 1$) in the octree tessellation we set the integration order to k_{max} . We then decrease the order between two levels in such a way that the degree is zero (a single integration point) at the finest octree levels $\varrho \geq \varrho_{\text{max}}$.

5. Immersed isogeometric analysis simulations

In this section we consider three applications of the topology-preserving image-based immersed isogeometric analysis technique presented above. In Section 5.1 we start with the case of a single-field problem in two dimensions by considering an elasticity problem. Subsequently, in Section 5.2 we consider a multi-field problem in the form of a Stokes flow through a carotid artery geometry. For this flow case we first consider a representative two-dimensional test case. The third application pertains to the extension of the Stokes flow case to a three-dimensional patient-specific geometry based on scan data. Let us note in advance that the carotid artery test case realistically pertains to moderate Reynolds number flows [113], but that a Stokes flow setting is here considered to focus on the topology-preserving analysis scheme developed in this work.

5.1. Uniaxial extension of a two-dimensional structure: a linear elasticity problem

We consider the two-dimensional specimen shown in Figure 19, which is represented by 32×32 grayscale voxels. The physical domain, Ω , with boundary $\partial\Omega$, is immersed into an ambient domain \mathcal{A} of (dimensionless) size $L \times L$ (with $L = 1$), with boundary $\partial\mathcal{A}$; see Figure 19c (with $\rho_{\max} = 3$). We consider a linear elasticity problem for which the displacement field, \mathbf{u} , is prescribed on the exterior (top and bottom) boundary, while the interior (immersed) boundary is traction free. In the absence of inertia effects and body forces, the boundary value problem reads as:

$$\left\{ \begin{array}{l} \text{Find } \mathbf{u} \text{ such that:} \\ \quad \text{div}(\boldsymbol{\sigma}(\mathbf{u})) = \mathbf{0} \quad \text{in } \Omega \\ \quad \mathbf{u} = \mathbf{0} \quad \text{on } \partial\mathcal{A}_0 \\ \quad \mathbf{u} = \bar{u}\mathbf{n} \quad \text{on } \partial\mathcal{A}_{\bar{u}} \\ \quad \mathbf{u} \cdot \mathbf{n} = 0 \quad \text{on } \partial\mathcal{A} \setminus (\partial\mathcal{A}_0 \cup \partial\mathcal{A}_{\bar{u}}) \\ \quad [\mathbf{I} - \mathbf{n} \otimes \mathbf{n}] \boldsymbol{\sigma} \mathbf{n} = \mathbf{0} \quad \text{on } \partial\mathcal{A} \setminus (\partial\mathcal{A}_0 \cup \partial\mathcal{A}_{\bar{u}}) \\ \quad \boldsymbol{\sigma} \mathbf{n} = \mathbf{0} \quad \text{on } \partial\Omega \setminus \partial\mathcal{A} \end{array} \right. \quad (41)$$

The various boundaries are specified in Figure 19b. The top boundary is displaced in normal direction by $\bar{u} = 0.2$ (20%). In the above problem definition, the stress is related to the strain by Hooke's law, *i.e.*, $\boldsymbol{\sigma}(\mathbf{u}) = \lambda \text{div}(\mathbf{u})\mathbf{I} + 2\mu \nabla^s \mathbf{u}$, where ∇^s denotes the symmetric gradient operator. Throughout this section, the non-dimensionalized Lamé parameters are set to $\lambda = \frac{1}{2}$ and $\mu = \frac{1}{2}$. In our analyses, as quantities of interest we consider the stress state in the specimen and the effective elastic modulus

$$\mathcal{Q} = \frac{L}{\bar{u}} \frac{1}{V_{\text{img}}} \int_{\Omega} \sigma_{22} \, dV. \quad (42)$$

In our simulations, the Dirichlet conditions on the external boundary are applied strongly, *i.e.*, by constraining the degrees of freedom related to the boundary displacements. This is enabled by the fact that the top and bottom boundaries are mesh conforming. The Galerkin problem corresponding to (41) then follows as

$$\left\{ \begin{array}{l} \text{Find } \mathbf{u}^h \in W^h(\Omega) \text{ such that for all } \mathbf{v}^h \in W_0^h(\Omega): \\ \int_{\Omega} \nabla^s \mathbf{v}^h : \boldsymbol{\sigma}(\mathbf{u}^h) \, dV = 0 \end{array} \right. \quad (43)$$

with the discrete spaces being subsets of $H^1(\Omega)$ satisfying the Dirichlet boundary conditions. The spaces are discretized using second-order ($k = 2$) B-spline basis functions defined on a background mesh with uniform element size h . For this setting, immersed analysis results can be obtained without additional stabilization terms.

In Figure 20 we present the results using a mesh size of $h = L/32$, which is equal to the voxel size. As can be seen in Figure 20, without application of the topology-correction algorithm (first column), the left connection (marked in green) is not reconstructed by the image segmentation procedure. As a result, the left side of the specimen carries only a small portion of the load, in the sense that (the vertical component of) the stress is equal to zero in the left part connected to the top boundary, and relatively small in the left section that is connected to the bottom boundary. When the topology-preservation algorithm is applied (second column in Figure 20), the left part of the structure remains connected, and the left side of the specimen is appropriately loaded.

From Figure 20 it is observed that the topological anomaly drastically affects the simulation results. When considering the effective elastic modulus (42), as shown in Figure 21 for various mesh sizes, it is observed that this quantity of interest shows fundamentally different behavior between the two considered cases. Since the topological anomaly occurs independently of the background-mesh element size, mesh refinement for the determination of the approximate solution does not repair this problem. Both solutions with and without the topological anomaly converge under mesh refinement, but the problem with the anomaly converges to an erroneous result on account of the incorrect geometry representation.

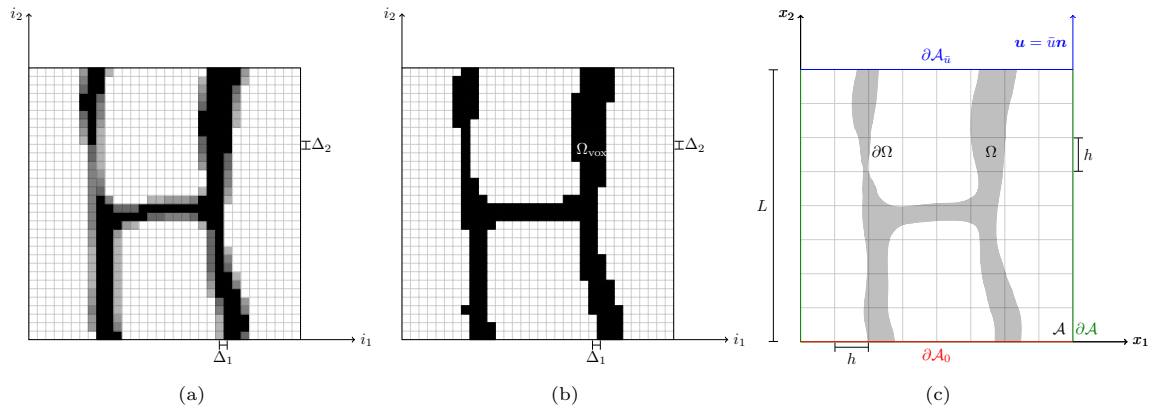


Figure 19: Illustration of (a) the original grayscale image, $g(\mathbf{x})$, (b) the voxel-segmentation of the image, i.e. $g(\mathbf{x}) > 0$, and (c) the computational domain (using $\varrho_{\max} = 3$) with the boundary conditions.

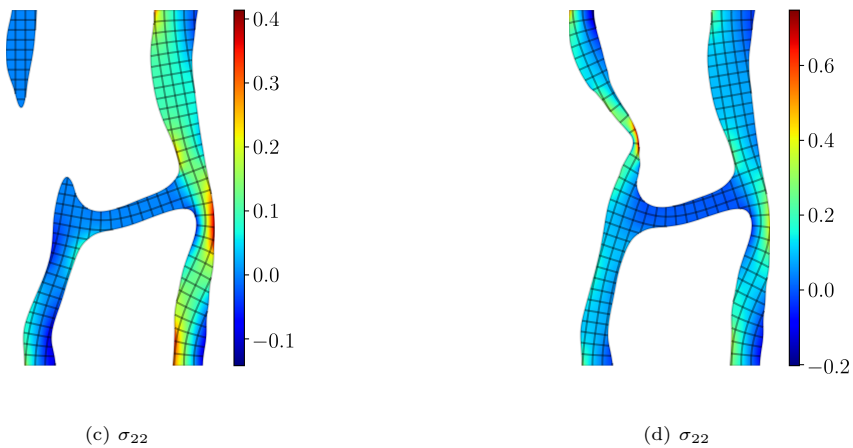
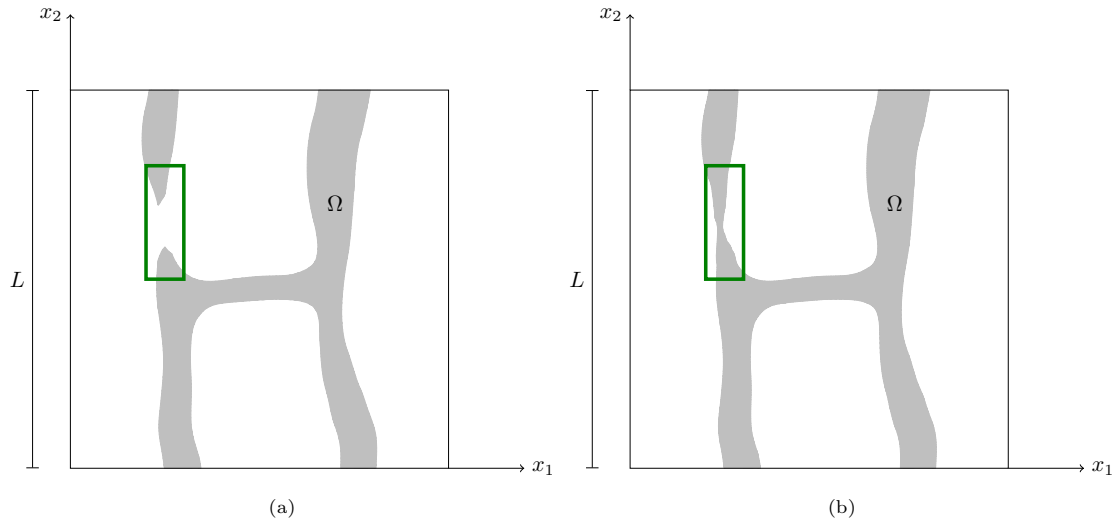


Figure 20: Comparison of the segmented geometry obtained from the grayscale image without (a) and with (b) topology preservation. The vertical (dimensionless) stress component for the two cases, computed using $h = L/32$, is shown in the panels (c) and (d).

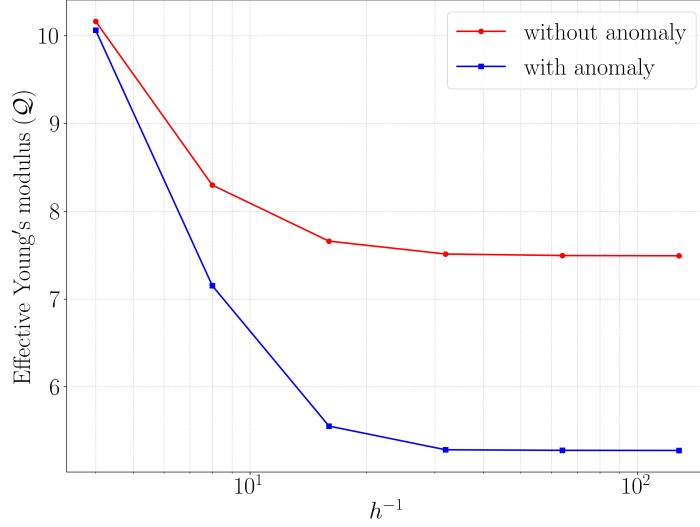


Figure 21: The effective elasticity modulus (42) computed with and without application of the topology-preservation technique for different mesh sizes h .

5.2. Flow through a carotid artery: a Stokes flow problem

We now consider Stokes flow through a domain $\Omega \subset \mathbb{R}^{n_d}$ ($n_d = 2, 3$), representative of a carotid artery. This domain is constructed using the topology-preserving segmentation procedure presented in Section 3, and is immersed in an ambient domain \mathcal{A} . We consider a pressure-driven incompressible flow of a Newtonian fluid, with viscosity μ , through the carotid artery. The fluid velocity, \mathbf{u} , and pressure, p , satisfy the strong formulation

$$\left\{ \begin{array}{l} \text{Find } \mathbf{u} \text{ and } p \text{ such that:} \\ -\nabla \cdot (2\mu \nabla^s \mathbf{u}) + \nabla p = \mathbf{0} \quad \text{in } \Omega \\ \nabla \cdot \mathbf{u} = 0 \quad \text{in } \Omega \\ \mathbf{u} = \mathbf{0} \quad \text{on } \Gamma_D = \partial\Omega \setminus \partial\mathcal{A} \\ (2\mu \nabla^s \mathbf{u} - p\mathbf{I}) \mathbf{n} = \mathbf{0} \quad \text{on } \partial\mathcal{A}_0 \\ (2\mu \nabla^s \mathbf{u} - p\mathbf{I}) \mathbf{n} = -\bar{p}\mathbf{n} \quad \text{on } \partial\mathcal{A}_{\bar{p}} \end{array} \right. \quad (44)$$

where \bar{p} denotes the pressure applied at the inflow (bottom) boundary.

The no-slip boundary condition on the immersed boundary Γ_D is imposed weakly through Nitsche's method. Ghost- and skeleton-stabilizations are used to avoid oscillations in the velocity and pressure fields (see Section 4). The mixed Galerkin form is given by

$$\left\{ \begin{array}{l} \text{Find } \mathbf{u}^h \in \mathbf{V}^h \text{ and } p^h \in Q^h \text{ such that:} \\ a(\mathbf{u}^h, \mathbf{v}^h) + b(p^h, \mathbf{v}^h) + s_{\text{ghost}}(\mathbf{u}^h, \mathbf{v}^h) = l(\mathbf{v}^h) \quad \forall \mathbf{v}^h \in \mathbf{V}^h \\ b(q^h, \mathbf{u}^h) - s_{\text{skeleton}}(p^h, q^h) = 0 \quad \forall q^h \in Q^h, \end{array} \right. \quad (45)$$

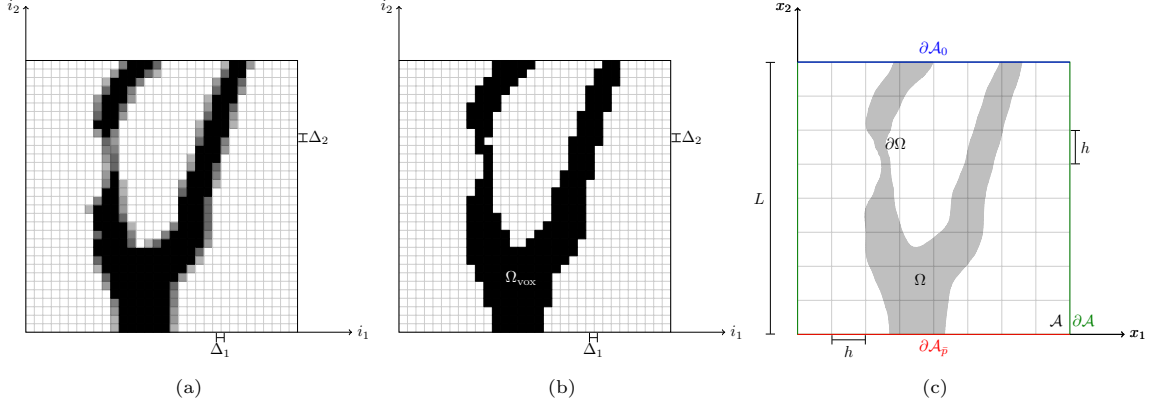


Figure 22: Illustration of (a) the original grayscale image, $g(\mathbf{x})$, (b) the voxel-segmentation of the image, i.e., $g(\mathbf{x}) > 0$, and (c) the computational domain (using $\varrho_{\max} = 3$) with the boundary conditions.

where the bilinear and linear operators are defined as [36]

$$a(\mathbf{u}^h, \mathbf{v}^h) := 2\mu(\nabla^s \mathbf{u}^h, \nabla^s \mathbf{v}^h) - 2\mu[\langle \nabla^s \mathbf{u}^h \cdot \mathbf{n}, \mathbf{v}^h \rangle_{\Gamma_D} + \langle \nabla^s \mathbf{v}^h \cdot \mathbf{n}, \mathbf{u}^h \rangle_{\Gamma_D}] + \langle \mu\beta h^{-1} \mathbf{u}^h, \mathbf{v}^h \rangle_{\Gamma_D} \quad (46a)$$

$$b(p^h, \mathbf{v}^h) := -(p^h, \operatorname{div} \mathbf{v}^h) \quad (46b)$$

$$l(\mathbf{v}^h) := -\langle \bar{p}, \mathbf{v}^h \cdot \mathbf{n} \rangle_{\partial \mathcal{A}_{\bar{p}}} \quad (46c)$$

$$s_{\text{skeleton}}(p^h, q^h) := \sum_{F \in \mathcal{F}_{\text{skeleton}}} \int_F \gamma \mu^{-1} h^{2k+1} \llbracket \partial_n^k p^h \rrbracket \llbracket \partial_n^k q^h \rrbracket \, dS \quad (46d)$$

$$s_{\text{ghost}}(\mathbf{u}^h, \mathbf{v}^h) := \sum_{F \in \mathcal{F}_{\text{ghost}}} \int_F \tilde{\gamma} \mu h^{2k-1} \llbracket \partial_n^k \mathbf{u}^h \rrbracket \cdot \llbracket \partial_n^k \mathbf{v}^h \rrbracket \, dS, \quad (46e)$$

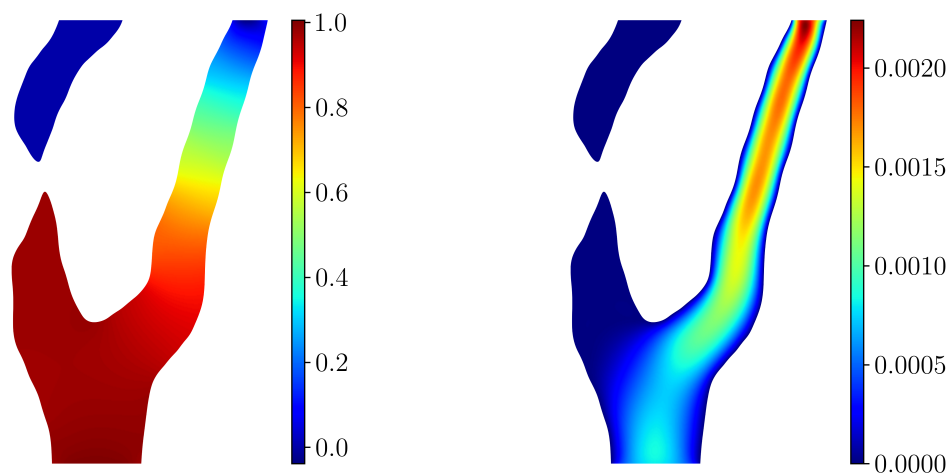
and (\cdot, \cdot) denotes the inner product in $L^2(\Omega)$, $\langle \cdot, \cdot \rangle_{\Gamma_D}$ denotes the inner product in $L^2(\Gamma_D)$, and $\llbracket \cdot \rrbracket$ is the jump operator. The parameters β , γ , and $\tilde{\gamma}$ denote the penalty constants for the Nitsche term, the Skeleton-stabilization term, and the Ghost-stabilization term, respectively. We consider second-order ($k = 2$) B-splines constructed on a variety of uniform background meshes with element size h . Let us note that we use equal-order approximations for the velocity and pressure fields, which is admissible by virtue of the skeleton-penalization acting on the pressure field.

5.2.1. Two-dimensional test case

To demonstrate the developed methodology in the Stokes flow case, we first consider the idealized two-dimensional geometry shown in Figure 22 (constructed from 32×32 grayscale voxels). In this two-dimensional case, we consider the ambient domain to be a unit square (with $L = 1$), and we set the non-dimensionalized parameters to $\mu = 1$ and $\bar{p} = 1$; see Figure 22c (constructed with $\varrho_{\max} = 3$). For the penalty parameters we take, $\beta = 100$, $\gamma = 0.05$, and $\tilde{\gamma} = 0.0005$, which have been determined empirically.

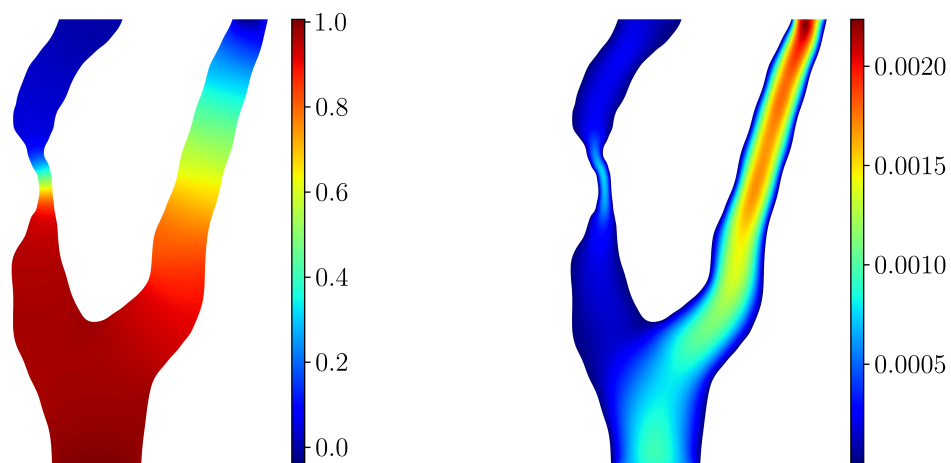
Figure 23 shows the pressure and velocity contour plots for the case where a topological anomaly occurs in the form of a pinched-off channel (top row), and in the case where the topology-preservation algorithm is applied (bottom row). The topological anomaly evidently obstructs fluid from flowing through the left branch, resulting in a zero pressure and zero fluid velocity solution in the top left disconnected domain. The topology-correction strategy proposed in this work avoids the left channel from being closed and results in a different flow profile. It is noteworthy that, if Dirichlet conditions were imposed on the top boundary, the pathological case without the topology-correction would have become singular.

The influence of the mesh size is studied in Figure 24, which, similar to the elasticity problem considered above, conveys that both simulation cases converge under mesh refinement. However, without application of the topology-correction strategy, the solution converges to an erroneous result.



(a) Pressure

(b) Velocity magnitude



(c) Pressure

(d) Velocity magnitude

Figure 23: Comparison of the pressure, p , and velocity magnitude, $|\mathbf{u}|$, for the segmented domain constructed without (top row) and with (bottom row) topology-preservation using $h = L/64$.

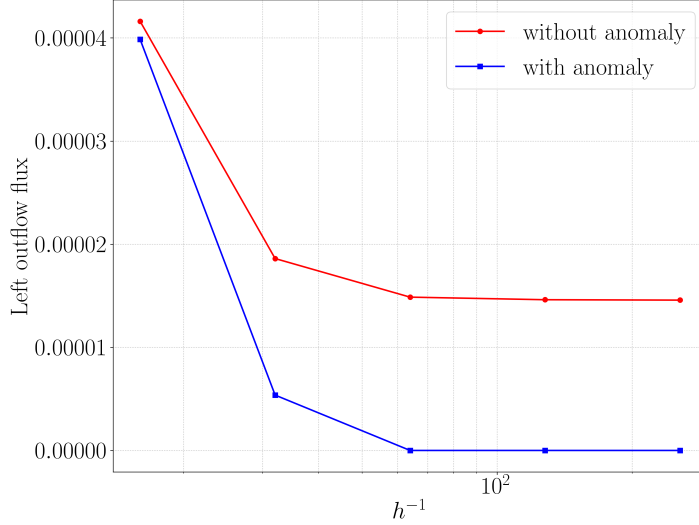


Figure 24: Total outflow from the left branch of the carotid artery, computed using different mesh sizes h , with and without the use of the topology-correction strategy.

5.2.2. Three-dimensional scan-based simulation

To demonstrate the developed methodology in a real scan-based setting, we consider a Stokes flow through a carotid artery. The geometry of the carotid artery is obtained from a CT-scan (see Figure 25). The scan data consists of 80 slices of 85×70 voxels. The size of the voxels is $300 \times 300 \mu\text{m}^2$ and the distance between the slices is $400 \mu\text{m}$. Hence, the total size of the scan domain is $25.6 \times 21.1 \times 32.0 \text{ mm}^3$. The original grayscale data, represented in DICOM format [113], is pre-processed using ITK-SNAP (open-source medical image processing tool [114]) from which binary voxel data is exported and read into our Python-based implementation of the developed topology-correction strategy.

The direct, non-smooth, segmentation of the image data is visualized in Figure 25a. When applying the spline-based segmentation procedure using second-order B-splines, the stenotic part of the artery in the original voxel image is lost (Figure 25b). As discussed in Section 2.2, this topological anomaly resulting from the spline-based segmentation procedure is expected on account of the feature-to-mesh-size ratio in that particular area.

In Figure 26 a zoom of the stenotic part of the artery is shown. Figure 26c shows the indicator function (21) as determined by the topology-correction strategy. This image conveys that the topological anomaly in the form of the missing stenotic part of the artery is appropriately detected. Figure 26d shows the smoothly segmented geometry after THB-spline refinement. From this figure it is observed that the topological anomaly is corrected by the proposed strategy. In the case of the complete topology (see Figure 25c), it is observed that additional boundary regions are tagged for refinement on account of the high-curvature of the boundary surface in these regions.

To simulate the flow through the stenotic artery we consider a viscosity of $\mu = 4 \text{ mPa s}$ and a pressure drop of 17.3 kPa (130 mm of Hg). These parameters are selected based on Ref. [113]. The penalty parameters associated with the weak formulation (45) are set to $\beta = 100$, $\gamma = 0.05$, and $\tilde{\gamma} = 0.0005$, which have been determined empirically to yield a stable formulation without adversely affecting the accuracy of the approximation.

The results for the velocity and pressure fields computed on a uniform mesh with $h = 1.75 \text{ mm}$ in the directions perpendicular to the pressure gradient and $h = 2 \text{ mm}$ in the direction of the pressure gradient are shown in Figure 27. Similar to the two-dimensional case, the topological anomaly evidently obstructs fluid from flowing through the stenotic part of the artery, resulting in a zero pressure and zero fluid velocity

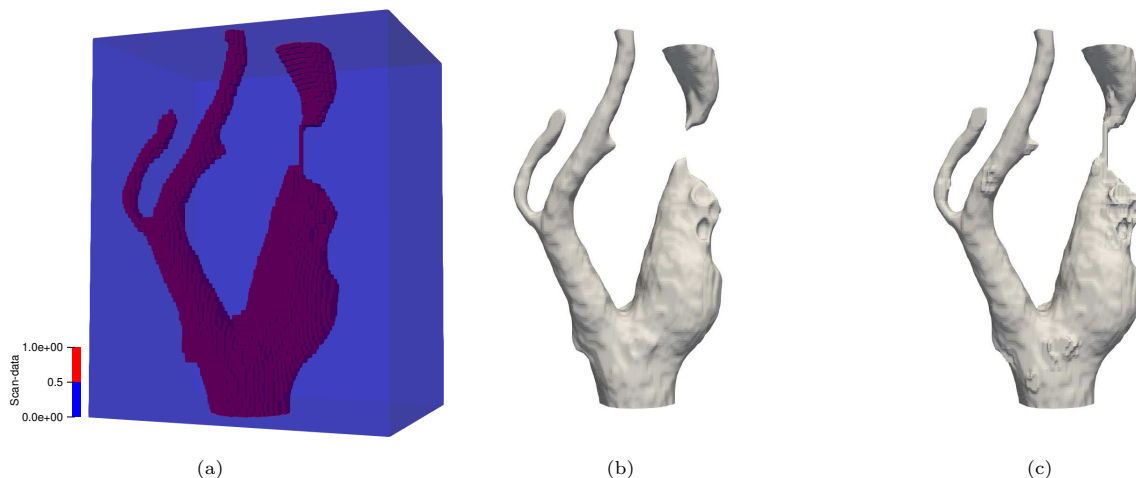


Figure 25: Illustration of (a) the directly segmented scan-data, $g(\mathbf{x})$. The computational domain of the stenotic carotid artery extracted by the B-spline-based segmentation procedure (b) before and (c) after application of the topology preservation algorithm. The smooth level set function, $f(\mathbf{x})$, is segmented using the midpoint tessellation procedure with a subdivision level of $q_{\max} = 2$.

solution in the right artery (see Figure 27). The topology-correction strategy avoids the stenotic part from being closed and results in a meaningful flow profile. Although the mesh considered here is relatively coarse, the flux through the stenotic region of approximately $200 \text{ mm}^3/\text{s}$ (corresponding to an average velocity of approximately 1.3 m/s , see Figure 27f) corresponds reasonably well with the flow through a circular tube (Hagen–Poiseuille flow) of length 8 mm and diameter 0.35 mm subject to the above-mentioned pressure drop, which corroborates that the computed speed is meaningful.

In Figure 28 the outflow through the stenotic branch of the artery is depicted for various uniform meshes, ranging from a very coarse mesh with $8,760$ (active) degrees of freedom to a refined mesh with $96,196$ degrees of freedom. Similar to the problems studied above, this mesh verification study conveys that both simulation cases converge under mesh refinement, but that an erroneous result is obtained in the case that the topology is not corrected. Note that, due to the employed uniform meshes, the number of degrees of freedom increases rapidly under mesh refinement, which will limit the size of the domain that can be considered by this type of analysis in practice. It is important to note, however, that mesh refinements throughout most of the domain do not substantially improve the accuracy of the simulation (in particular for the considered quantity of interest). Therefore, to properly leverage the property of immersed techniques that the mesh resolution can be controlled independently of the geometry (and topology) representation, significant improvements in computational efficiency can be obtained by means of adaptive local mesh refinement. The combination of the proposed technique with an error-estimation-and-adaptivity strategy is an important topic of further study.

6. Concluding remarks

To leverage the advantageous properties of isogeometric analysis in a scan-based setting, a smooth representation of the computational domain must be obtained. This can be achieved by applying a smoothing operation on the voxel-based gray-scale data and subsequently applying an octree-based tessellation procedure. A negative side-effect of this smoothing procedure is that it can induce topological changes when the scan data contains features with a characteristic length scale similar to the voxel size.

Based on a Fourier analysis of the B-spline-based smoothing operation, it is proposed to repair smoothing-induced topological anomalies by locally refining the smoothed gray-scale function using THB-splines. In combination with a moving-window strategy to detect topological changes, the local refinement technique is used to develop a topology-preserving image segmentation technique. Based on a comparison of the Euler

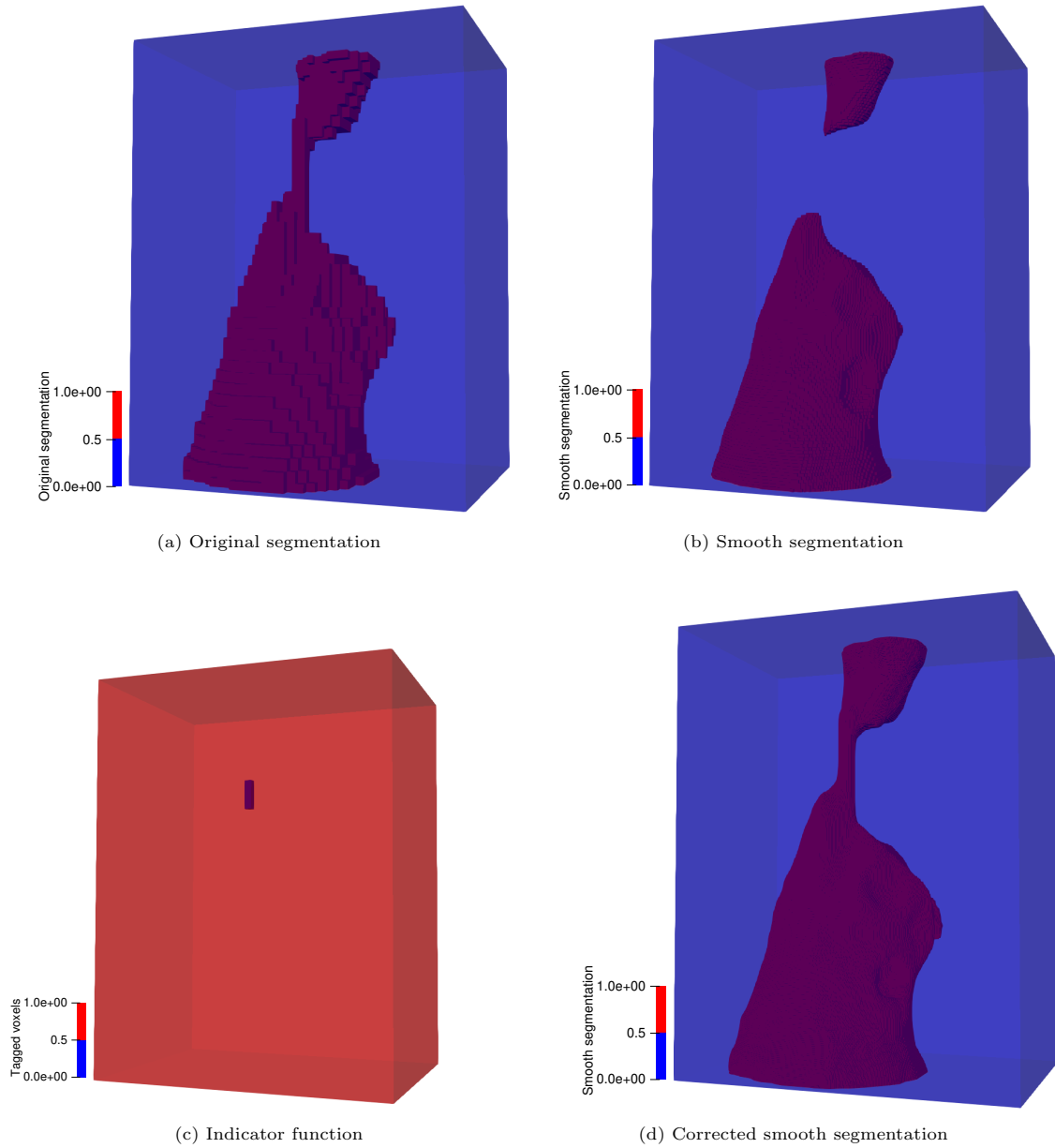


Figure 26: Illustration of the topology-preserving procedure focused on the stenotic part of the carotid artery. Panel (a) shows the original segmentation obtained directly by thresholding the voxel data, and panel (b) shows the segmentation through the B-spline-based smoothing strategy. A moving-window technique then locally compares the topology between the two segmentations, which results in the indicator function (c) that marks topological differences. THB-spline-based refinements are then introduced to locally increase the resolution of the smooth level set function, thereby preserving the topology of the original scan-data (d).

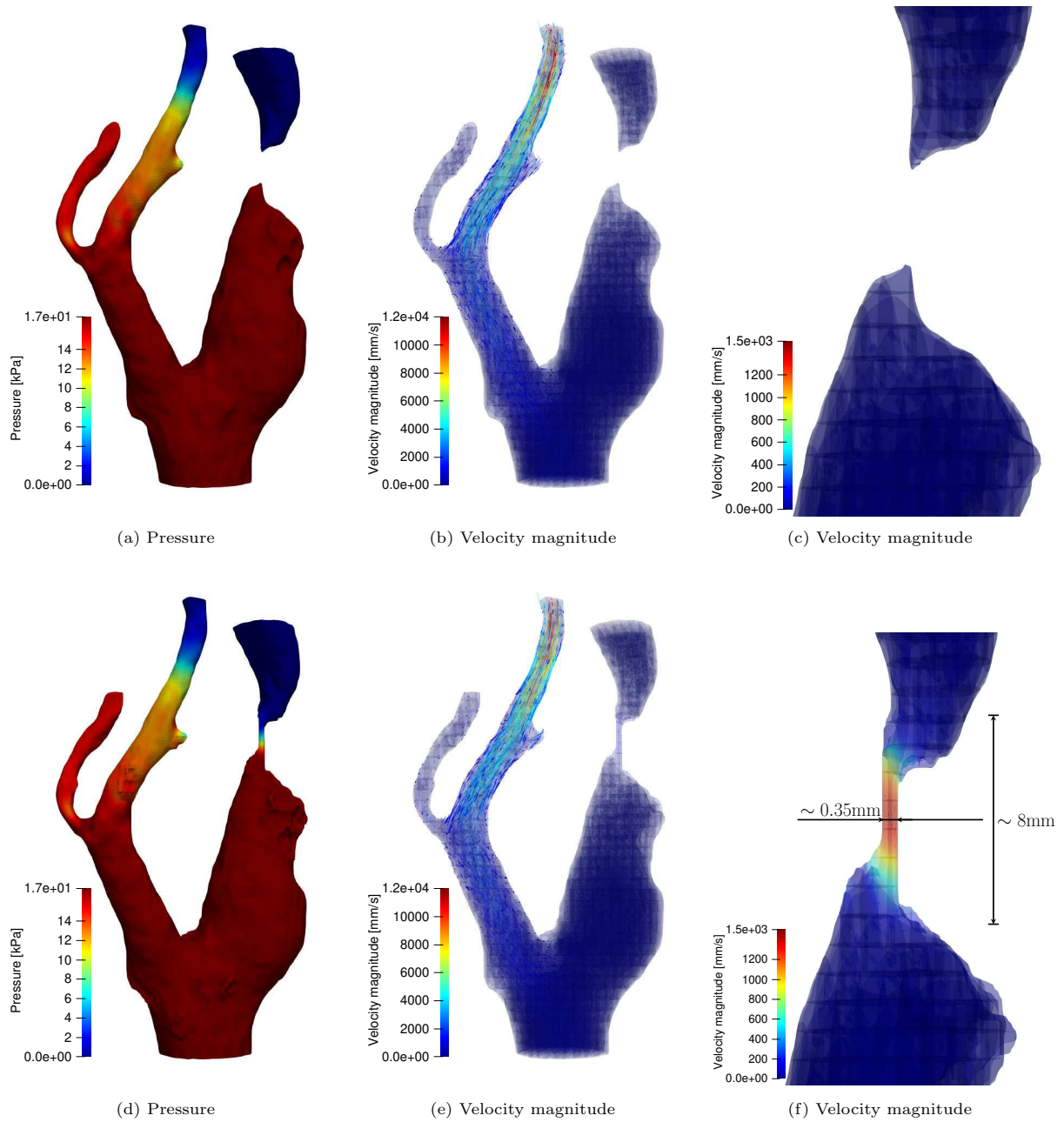


Figure 27: Comparison of the pressure, p , and velocity magnitude, $|\mathbf{u}|$, for the segmented domain constructed without (top row) and with (bottom row) topology-preservation using a mesh size of $h = 2$ mm in the vertical direction, and $h = 1.75$ mm in the other directions.

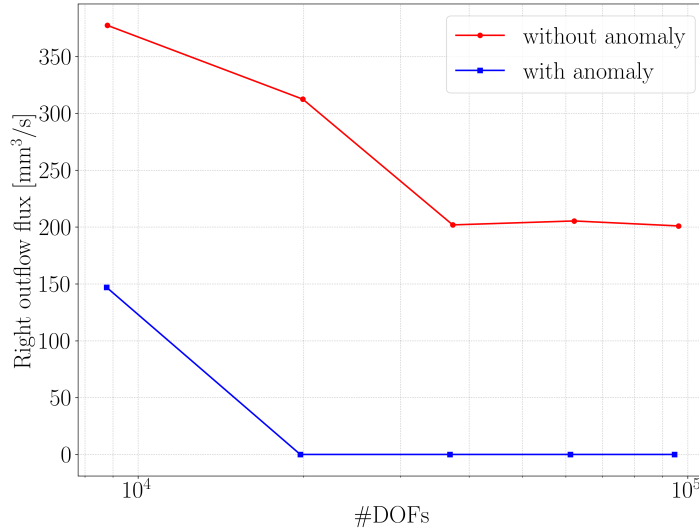


Figure 28: Total outflow from the right branch of the carotid artery, computed using different degrees of freedom (DOFs), with and without the use of the topology-correction strategy.

characteristic between the window view on the original voxel data and that on the smoothed representation, the proposed technique systematically distinguishes shape changes from topological changes. The algorithm is fail-safe in that it detects and repairs topological changes, and does not essentially change the geometry in the (rare) case that a shape change is accidentally marked for refinement. The proposed location-based masking strategy to detect shape changes is very effective for the considered test cases, but it is envisioned that further robustness improvements can be made by the development of a more advanced masking procedure.

The developed algorithm works for two- and three-dimensional scan data. Numerical simulations demonstrate the effectivity of the algorithm in both settings. For all considered test cases, a topologically consistent smoothed image is obtained after a single topology-correction step. Based on the presented Fourier analysis this is to be expected, as refining the mesh for the B-spline grayscale function has a strong effect on the filtering properties. It can, in principle, occur that topological changes are not repaired after a single correction step. Although not considered in this work, the presented algorithm has the potential to be extended so that it can be applied recursively in such scenarios.

In this work we have restricted ourselves to immersed isogeometric analyses based on uniform meshes. In order to optimally benefit from the fact that the computational mesh is decoupled from the segmented geometry in the immersed setting, use should be made of (adaptive) local refinements for the analysis mesh. Combination of the proposed topology-preservation technique with an adaptive meshing strategy is therefore an important topic of further study.

Acknowledgement

We acknowledge the support from the European Commission EACEA Agency, Framework Partnership Agreement 2013-0043 Erasmus Mundus Action 1b, as a part of the EM Joint Doctorate Simulation in Engineering and Entrepreneurship Development (SEED). A.R. acknowledges the partial support of the MIUR-PRIN project XFAST-SIMS (no. 20173C478N). All the simulations in this work were performed based on the open source software package Nutils (www.nutills.org) [111]. We acknowledge the support of the Nutils team. We acknowledge Michele Conti for providing the CT-scan data of the stenotic carotid and Alice Finotello for the help in understanding the data.

References

- [1] J. A. Cottrell, T. J. R. Hughes, Y. Bazilevs, *Isogeometric analysis: Toward integration of CAD and FEA*, John Wiley & Sons, 2009.
- [2] T. J. R. Hughes, J. A. Cottrell, Y. Bazilevs, *Isogeometric analysis: CAD, finite elements, NURBS, exact geometry and mesh refinement*, *Computer Methods in Applied Mechanics and Engineering* 194 (39-41) (2005) 4135–4195.
- [3] Y. Zhang, Y. Bazilevs, S. Goswami, C. L. Bajaj, T. J. R. Hughes, *Patient-specific vascular NURBS modeling for isogeometric analysis of blood flow*, *Computer Methods in Applied Mechanics and Engineering* 196 (29-30) (2007) 2943–2959.
- [4] S. Morganti, F. Auricchio, D. Benson, F. Gambarin, S. Hartmann, T. J. R. Hughes, A. Reali, *Patient-specific isogeometric structural analysis of aortic valve closure*, *Computer Methods in Applied Mechanics and Engineering* 284 (2015) 508–520.
- [5] T. Hoang, C. V. Verhoosel, F. Auricchio, E. H. van Brummelen, A. Reali, *Skeleton-stabilized isogeometric analysis: High-regularity interior-penalty methods for incompressible viscous flow problems*, *Computer Methods in Applied Mechanics and Engineering* 337 (2018) 324–351.
- [6] S. Marschke, L. Wunderlich, W. Ring, K. Achterhold, F. Pfeiffer, *An approach to construct a three-dimensional isogeometric model from μ -CT scan data with an application to the bridge of a violin*, *Computer Aided Geometric Design* 78 (2020) 101815.
- [7] B. van Rietbergen, H. Weinans, R. Huiskes, B. Polman, *Computational strategies for iterative solutions of large FEM applications employing voxel data*, *International Journal for Numerical Methods in Engineering* 39 (16) (1996) 2743–2767.
- [8] D. Rajon, W. E. Bolch, *Marching cube algorithm: review and trilinear interpolation adaptation for image-based dosimetric models*, *Computerized Medical Imaging and Graphics* 27 (5) (2003) 411–435.
- [9] Z. Wang, J. C. M. Teo, C. K. Chui, S. H. Ong, C. H. Yan, S. Wang, H. K. Wong, S. H. Teoh, *Computational biomechanical modelling of the lumbar spine using marching-cubes surface smoothed finite element voxel meshing*, *Computer Methods and Programs in Biomedicine* 80 (1) (2005) 25–35.
- [10] Y. Bazilevs, V. M. Calo, Y. Zhang, T. J. R. Hughes, *Isogeometric fluid–structure interaction analysis with applications to arterial blood flow*, *Computational Mechanics* 38 (4) (2006) 310–322.
- [11] Y. Bazilevs, J. Gohean, T. J. R. Hughes, R. Moser, Y. Zhang, *Patient-specific isogeometric fluid–structure interaction analysis of thoracic aortic blood flow due to implantation of the Jarvik 2000 left ventricular assist device*, *Computer Methods in Applied Mechanics and Engineering* 198 (45-46) (2009) 3534–3550.
- [12] Y. Yu, Y. J. Zhang, K. Takizawa, T. E. Tezduyar, T. Sasaki, *Anatomically realistic lumen motion representation in patient-specific space–time isogeometric flow analysis of coronary arteries with time-dependent medical-image data*, *Computational Mechanics* 65 (2) (2020) 395–404.
- [13] B. Urick, T. M. Sanders, S. S. Hossain, Y. J. Zhang, T. J. R. Hughes, *Review of patient-specific vascular modeling: template-based isogeometric framework and the case for CAD*, *Archives of Computational Methods in Engineering* 26 (2) (2019) 381–404.
- [14] T. Martin, E. Cohen, R. M. Kirby, *Volumetric parameterization and trivariate B-spline fitting using harmonic functions*, *Computer Aided Geometric Design* 26 (6) (2009) 648–664.
- [15] F. Auricchio, M. Conti, M. Ferraro, S. Morganti, A. Reali, R. Taylor, *Innovative and efficient stent flexibility simulations based on isogeometric analysis*, *Computer Methods in Applied Mechanics and Engineering* 295 (2015) 347–361.
- [16] M. S. Pigazzini, Y. Bazilevs, A. Ellison, H. Kim, *Isogeometric analysis for simulation of progressive damage in composite laminates*, *Journal of Composite Materials* 52 (25) (2018) 3471–3489.
- [17] M. Bucelli, M. Salvador, L. Dede, A. Quarteroni, *Multipatch isogeometric analysis for electrophysiology: Simulation in a human heart*, *Computer Methods in Applied Mechanics and Engineering* 376 (2021) 113666.
- [18] T. Terahara, K. Takizawa, T. E. Tezduyar, Y. Bazilevs, M. C. Hsu, *Heart valve isogeometric sequentially-coupled FSI analysis with the space–time topology change method*, *Computational Mechanics* (2020) 1–21.
- [19] C. V. Verhoosel, G. van Zwieten, B. van Rietbergen, R. de Borst, *Image-based goal-oriented adaptive isogeometric analysis with application to the micro-mechanical modeling of trabecular bone*, *Computer Methods in Applied Mechanics and Engineering* 284 (2015) 138–164.
- [20] E. Rank, M. Ruess, S. Kollmannsberger, D. Schillinger, A. Düster, *Geometric modeling, isogeometric analysis and the finite cell method*, *Computer Methods in Applied Mechanics and Engineering* 249 (2012) 104–115.
- [21] D. Schillinger, L. Dede, M. A. Scott, J. A. Evans, M. J. Borden, E. Rank, T. J. R. Hughes, *An isogeometric design-through-analysis methodology based on adaptive hierarchical refinement of NURBS, immersed boundary methods, and T-spline CAD surfaces*, *Computer Methods in Applied Mechanics and Engineering* 249 (2012) 116–150.
- [22] M. Ruess, D. Tal, N. Trabelsi, Z. Yosibash, E. Rank, *The finite cell method for bone simulations: verification and validation*, *Biomechanics and Modeling in Mechanobiology* 11 (3) (2012) 425–437.
- [23] M. Ruess, D. Schillinger, Y. Bazilevs, V. Varduhn, E. Rank, *Weakly enforced essential boundary conditions for NURBS-embedded and trimmed NURBS geometries on the basis of the finite cell method*, *International Journal for Numerical Methods in Engineering* 95 (10) (2013) 811–846.
- [24] D. Schillinger, M. Ruess, *The finite cell method: A review in the context of higher-order structural analysis of CAD and image-based geometric models*, *Archives of Computational Methods in Engineering* 22 (3) (2015) 391–455.
- [25] M. C. Hsu, C. Wang, F. Xu, A. J. Herrema, A. Krishnamurthy, *Direct immersogeometric fluid flow analysis using B-rep CAD models*, *Computer Aided Geometric Design* 43 (2016) 143–158.
- [26] A. Düster, J. Parvizian, Z. Yang, E. Rank, *The finite cell method for three-dimensional problems of solid mechanics*, *Computer Methods in Applied Mechanics and Engineering* 197 (45-48) (2008) 3768–3782.

- [27] D. Schillinger, M. Ruess, N. Zander, Y. Bazilevs, A. Düster, E. Rank, Small and large deformation analysis with the p - and B-spline versions of the finite cell method, *Computational Mechanics* 50 (4) (2012) 445–478.
- [28] M. Elhaddad, N. Zander, T. Bog, L. Kudela, S. Kollmannsberger, J. Kirschke, T. Baum, M. Ruess, E. Rank, Multi-level hp -finite cell method for embedded interface problems with application in biomechanics, *International Journal for Numerical Methods in Biomedical Engineering* 34 (4) (2018) e2951.
- [29] M. Würkner, S. Duczek, H. Berger, H. Köppe, U. Gabbert, A software platform for the analysis of porous die-cast parts using the finite cell method, in: *Analysis and Modelling of Advanced Structures and Smart Systems*, Springer, 2018, pp. 327–341.
- [30] S. Duczek, H. Berger, U. Gabbert, The finite pore method: a new approach to evaluate gas pores in cast parts by combining computed tomography and the finite cell method, *International Journal of Cast Metals Research* 28 (4) (2015) 221–228.
- [31] H. J. Kim, Y. D. Seo, S. K. Youn, Isogeometric analysis for trimmed CAD surfaces, *Computer Methods in Applied Mechanics and Engineering* 198 (37–40) (2009) 2982–2995.
- [32] H. J. Kim, Y. D. Seo, S. K. Youn, Isogeometric analysis with trimming technique for problems of arbitrary complex topology, *Computer Methods in Applied Mechanics and Engineering* 199 (45–48) (2010) 2796–2812.
- [33] R. Schmidt, R. Wüchner, K. U. Bletzinger, Isogeometric analysis of trimmed NURBS geometries, *Computer Methods in Applied Mechanics and Engineering* 241 (2012) 93–111.
- [34] F. de Prenter, C. V. Verhoosel, E. H. van Brummelen, J. A. Evans, C. Messe, J. Benzaken, K. Maute, Multigrid solvers for immersed finite element methods and immersed isogeometric analysis, *Computational Mechanics* 65 (3) (2020) 807–838.
- [35] A. Düster, H. G. Sehlhorst, E. Rank, Numerical homogenization of heterogeneous and cellular materials utilizing the finite cell method, *Computational Mechanics* 50 (4) (2012) 413–431.
- [36] T. Hoang, C. V. Verhoosel, C. Z. Qin, F. Auricchio, A. Reali, E. H. van Brummelen, Skeleton-stabilized immersogeometric analysis for incompressible viscous flow problems, *Computer Methods in Applied Mechanics and Engineering* 344 (2019) 421–450.
- [37] J. N. Jomo, F. de Prenter, M. Elhaddad, D. D’Angella, C. V. Verhoosel, S. Kollmannsberger, J. S. Kirschke, V. Nübel, E. H. van Brummelen, E. Rank, Robust and parallel scalable iterative solutions for large-scale finite cell analyses, *Finite Elements in Analysis and Design* 163 (2019) 14–30.
- [38] M. Carraturo, J. N. Jomo, S. Kollmannsberger, A. Reali, F. Auricchio, E. Rank, Modeling and experimental validation of an immersed thermo-mechanical part-scale analysis for laser powder bed fusion processes, *Additive Manufacturing* 36 (2020) 101498.
- [39] M. C. Hsu, D. Kamensky, Y. Bazilevs, M. S. Sacks, T. J. R. Hughes, Fluid–structure interaction analysis of bioprosthetic heart valves: significance of arterial wall deformation, *Computational Mechanics* 54 (4) (2014) 1055–1071.
- [40] D. Kamensky, M. C. Hsu, D. Schillinger, J. A. Evans, A. Aggarwal, Y. Bazilevs, M. S. Sacks, T. J. R. Hughes, An immer- sogeometric variational framework for fluid–structure interaction: Application to bioprosthetic heart valves, *Computer Methods in Applied Mechanics and Engineering* 284 (2015) 1005–1053.
- [41] D. Kamensky, M. C. Hsu, Y. Yu, J. A. Evans, M. S. Sacks, T. J. R. Hughes, Immersogeometric cardiovascular fluid– structure interaction analysis with divergence-conforming B-splines, *Computer Methods in Applied Mechanics and Engineering* 314 (2017) 408–472.
- [42] L. Kudela, N. Zander, T. Bog, S. Kollmannsberger, E. Rank, Efficient and accurate numerical quadrature for immersed boundary methods, *Advanced Modeling and Simulation in Engineering Sciences* 2 (1) (2015) 1–22.
- [43] L. Kudela, N. Zander, S. Kollmannsberger, E. Rank, Smart octrees: Accurately integrating discontinuous functions in 3D, *Computer Methods in Applied Mechanics and Engineering* 306 (2016) 406–426.
- [44] M. Joulaiian, S. Hubrich, A. Düster, Numerical integration of discontinuities on arbitrary domains based on moment fitting, *Computational Mechanics* 57 (6) (2016) 979–999.
- [45] S. C. Divi, C. V. Verhoosel, F. Auricchio, A. Reali, E. H. van Brummelen, Error-estimate-based adaptive integration for immersed isogeometric analysis, *Computers & Mathematics with Applications* 80 (11) (2020) 2481–2516.
- [46] J. Nitsche, Über ein variationsprinzip zur lösung von dirichlet-problemen bei verwendung von teilräumen, die keinen randbedingungen unterworfen sind, in: *Abhandlungen aus dem Mathematischen Seminar der Universität Hamburg*, Vol. 36, Springer, 1971, pp. 9–15.
- [47] A. Hansbo, P. Hansbo, An unfitted finite element method, based on Nitsche’s method, for elliptic interface problems, *Computer Methods in Applied Mechanics and Engineering* 191 (47–48) (2002) 5537–5552.
- [48] A. Embar, J. Dolbow, I. Harari, Imposing dirichlet boundary conditions with Nitsche’s method and spline-based finite elements, *International Journal for Numerical Methods in Engineering* 83 (7) (2010) 877–898.
- [49] T. Boiveau, E. Burman, A penalty-free Nitsche method for the weak imposition of boundary conditions in compressible and incompressible elasticity, *IMA Journal of Numerical Analysis* 36 (2) (2016) 770–795.
- [50] E. Burman, P. Hansbo, Fictitious domain finite element methods using cut elements: II. a stabilized Nitsche method, *Applied Numerical Mathematics* 62 (4) (2012) 328–341.
- [51] E. Burman, P. Hansbo, Fictitious domain methods using cut elements: III. a stabilized Nitsche method for stokes’ problem, *ESAIM: Mathematical Modelling and Numerical Analysis* 48 (3) (2014) 859–874.
- [52] F. de Prenter, C. Lehrenfeld, A. Massing, A note on the stability parameter in Nitsche’s method for unfitted boundary value problems, *Computers & Mathematics with Applications* 75 (12) (2018) 4322–4336.
- [53] F. de Prenter, C. V. Verhoosel, G. van Zwieten, E. H. van Brummelen, Condition number analysis and preconditioning of the finite cell method, *Computer Methods in Applied Mechanics and Engineering* 316 (2017) 297–327.
- [54] E. Burman, Ghost penalty, *Comptes Rendus Mathématique* 348 (21–22) (2010) 1217–1220.
- [55] E. Burman, M. A. Fernández, An unfitted Nitsche method for incompressible fluid–structure interaction using overlapping

- meshes, *Computer Methods in Applied Mechanics and Engineering* 279 (2014) 497–514.
- [56] W. Dettmer, C. Kadapa, D. Perić, A stabilised immersed boundary method on hierarchical B-spline grids, *Computer Methods in Applied Mechanics and Engineering* 311 (2016) 415–437.
- [57] S. Badia, F. Verdugo, A. F. Martín, The aggregated unfitted finite element method for elliptic problems, *Computer Methods in Applied Mechanics and Engineering* 336 (2018) 533–553.
- [58] F. de Prenter, C. V. Verhoosel, E. H. van Brummelen, Preconditioning immersed isogeometric finite element methods with application to flow problems, *Computer Methods in Applied Mechanics and Engineering* 348 (2019) 604–631.
- [59] M. Ruess, D. Schillinger, A. I. Oezcan, E. Rank, Weak coupling for isogeometric analysis of non-matching and trimmed multi-patch geometries, *Computer Methods in Applied Mechanics and Engineering* 269 (2014) 46–71.
- [60] A. Düster, E. Rank, B. Szabó, The p -version of the finite element and finite cell methods, *Encyclopedia of Computational Mechanics Second Edition* (2017) 1–35.
- [61] D. Schillinger, E. Rank, An unfitted hp -adaptive finite element method based on hierarchical B-splines for interface problems of complex geometry, *Computer Methods in Applied Mechanics and Engineering* 200 (47-48) (2011) 3358–3380.
- [62] D. Schillinger, A. Düster, E. Rank, The hp - d -adaptive finite cell method for geometrically nonlinear problems of solid mechanics, *International Journal for Numerical Methods in Engineering* 89 (9) (2012) 1171–1202.
- [63] S. Heinze, M. Joulaian, A. Düster, Numerical homogenization of hybrid metal foams using the finite cell method, *Computers & Mathematics with Applications* 70 (7) (2015) 1501–1517.
- [64] W. Garhuom, S. Hubrich, L. Radtke, A. Düster, A remeshing strategy for large deformations in the finite cell method, *Computers & Mathematics with Applications* 80 (11) (2020) 2379–2398.
- [65] J. F. Mangin, V. Frouin, I. Bloch, J. Régis, J. López-Krahe, From 3D magnetic resonance images to structural representations of the cortex topography using topology preserving deformations, *Journal of Mathematical Imaging and Vision* 5 (4) (1995) 297–318.
- [66] A. M. Dale, B. Fischl, M. I. Sereno, Cortical surface-based analysis: I. segmentation and surface reconstruction, *Neuroimage* 9 (2) (1999) 179–194.
- [67] C. Xu, D. L. Pham, M. E. Rettmann, D. N. Yu, J. L. Prince, Reconstruction of the human cerebral cortex from magnetic resonance images, *IEEE Transactions on Medical Imaging* 18 (6) (1999) 467–480.
- [68] B. Fischl, A. Liu, A. M. Dale, Automated manifold surgery: constructing geometrically accurate and topologically correct models of the human cerebral cortex, *IEEE Transactions on Medical Imaging* 20 (1) (2001) 70–80.
- [69] F. Ségonne, J. Pacheco, B. Fischl, Geometrically accurate topology-correction of cortical surfaces using nonseparating loops, *IEEE Transactions on Medical Imaging* 26 (4) (2007) 518–529.
- [70] H. Lester, S. R. Arridge, A survey of hierarchical non-linear medical image registration, *Pattern Recognition* 32 (1) (1999) 129–149.
- [71] Z. Xie, G. E. Farin, Image registration using hierarchical B-splines, *IEEE Transactions on Visualization and Computer Graphics* 10 (1) (2004) 85–94.
- [72] A. Pawar, Y. J. Zhang, C. Anitescu, T. Rabczuk, Joint image segmentation and registration based on a dynamic level set approach using truncated hierarchical B-splines, *Computers & Mathematics with Applications* 78 (10) (2019) 3250–3267.
- [73] G. Falqui, C. Reina, BRS cohomology and topological anomalies, *Communications in Mathematical Physics* 102 (3) (1985) 503–515.
- [74] T. Qaiser, K. Sirinukunwattana, K. Nakane, Y. W. Tsang, D. Epstein, N. Rajpoot, Persistent homology for fast tumor segmentation in whole slide histology images, *Procedia Computer Science* 90 (2016) 119–124.
- [75] W. Bae, J. Yoo, J. Chul Ye, Beyond deep residual learning for image restoration: Persistent homology-guided manifold simplification, in: *Proceedings of the IEEE Conference on Computer Vision and Pattern Recognition Workshops, 2017*, pp. 145–153.
- [76] R. Assaf, A. Goupil, V. Vrabie, T. Boudier, M. Kacim, Persistent homology for object segmentation in multidimensional grayscale images, *Pattern Recognition Letters* 112 (2018) 277–284.
- [77] X. Hu, L. Fuxin, D. Samaras, C. Chen, Topology-preserving deep image segmentation, *arXiv preprint arXiv:1906.05404*.
- [78] J. Clough, N. Byrne, I. Oksuz, V. A. Zimmer, J. A. Schnabel, A. King, A topological loss function for deep-learning based image segmentation using persistent homology, *IEEE Transactions on Pattern Analysis and Machine Intelligence*.
- [79] P. de Dumast, H. Kebiri, C. Atat, V. Dunet, M. Koob, M. B. Cuadra, Segmentation of the cortical plate in fetal brain MRI with a topological loss, *arXiv preprint arXiv:2010.12391*.
- [80] N. Byrne, J. R. Clough, G. Montana, A. P. King, A persistent homology-based topological loss function for multi-class CNN segmentation of cardiac mri, *arXiv preprint arXiv:2008.09585*.
- [81] A. A. Novotny, R. A. Feijóo, E. Taroco, C. Padra, Topological sensitivity analysis, *Computer Methods in Applied Mechanics and Engineering* 192 (7-8) (2003) 803–829.
- [82] M. Burger, B. Hackl, W. Ring, Incorporating topological derivatives into level set methods, *Journal of Computational Physics* 194 (1) (2004) 344–362.
- [83] L. He, C. Y. Kao, S. Osher, Incorporating topological derivatives into shape derivatives based level set methods, *Journal of Computational Physics* 225 (1) (2007) 891–909.
- [84] I. Larrabide, R. Feijóo, A. Novotny, E. Taroco, Topological derivative: a tool for image processing, *Computers & Structures* 86 (13-14) (2008) 1386–1403.
- [85] M. Hintermüller, A. Laurain, Multiphase image segmentation and modulation recovery based on shape and topological sensitivity, *Journal of Mathematical Imaging and Vision* 35 (1) (2009) 1–22.
- [86] M. Droske, B. Meyer, M. Rumpf, C. Schaller, An adaptive level set method for medical image segmentation, in: *Biennial International Conference on Information Processing in Medical Imaging, Springer, 2001*, pp. 416–422.
- [87] V. Sochnikov, S. Efrima, Level set calculations of the evolution of boundaries on a dynamically adaptive grid, *International*

- Journal for Numerical Methods in Engineering 56 (13) (2003) 1913–1929.
- [88] M. Xu, P. M. Thompson, A. W. Toga, An adaptive level set segmentation on a triangulated mesh, *IEEE Transactions on Medical Imaging* 23 (2) (2004) 191–201.
 - [89] G. Varadhan, S. Krishnan, T. Sriram, D. Manocha, Topology preserving surface extraction using adaptive subdivision, in: *Proceedings of the 2004 Eurographics/ACM SIGGRAPH Symposium on Geometry Processing*, 2004, pp. 235–244.
 - [90] Y. Bai, X. Han, J. L. Prince, Octree-based topology-preserving isosurface simplification, in: *2006 Conference on Computer Vision and Pattern Recognition Workshop (CVPRW'06)*, IEEE, 2006, pp. 81–81.
 - [91] Y. Bai, X. Han, J. L. Prince, Octree grid topology preserving geometric deformable model for three-dimensional medical image segmentation, in: *Biennial International Conference on Information Processing in Medical Imaging*, Springer, 2007, pp. 556–568.
 - [92] C. Giannelli, B. Jüttler, H. Speleers, THB-splines: The truncated basis for hierarchical splines, *Computer Aided Geometric Design* 29 (7) (2012) 485–498.
 - [93] D. D’Angella, S. Kollmannsberger, E. Rank, A. Reali, Multi-level Bézier extraction for hierarchical local refinement of isogeometric analysis, *Computer Methods in Applied Mechanics and Engineering* 328 (2018) 147–174.
 - [94] D. D’Angella, A. Reali, Efficient extraction of hierarchical B-splines for local refinement and coarsening of isogeometric analysis, *Computer Methods in Applied Mechanics and Engineering* 367 (2020) 113131.
 - [95] X. Han, C. Xu, J. L. Prince, A topology preserving level set method for geometric deformable models, *IEEE Transactions on Pattern Analysis and Machine Intelligence* 25 (6) (2003) 755–768.
 - [96] H. Lee, H. Kang, M. K. Chung, B. N. Kim, D. S. Lee, Persistent brain network homology from the perspective of dendrogram, *IEEE Transactions on Medical Imaging* 31 (12) (2012) 2267–2277.
 - [97] D. Lee, J. Yoo, J. C. Ye, Deep residual learning for compressed sensing MRI, in: *2017 IEEE 14th International Symposium on Biomedical Imaging (ISBI 2017)*, IEEE, 2017, pp. 15–18.
 - [98] L. Piegl, W. Tiller, Curve and surface constructions using rational B-splines, *Computer-Aided Design* 19 (9) (1987) 485–498.
 - [99] L. Shapiro, *Computer vision and image processing*, Academic Press, 1992.
 - [100] L. Ortiz-Gracia, C. W. Oosterlee, A highly efficient shannon wavelet inverse fourier technique for pricing european options, *SIAM Journal on Scientific Computing* 38 (1) (2016) B118–B143.
 - [101] J. Long, E. Shelhamer, T. Darrell, Fully convolutional networks for semantic segmentation, in: *Proceedings of the IEEE Conference on Computer Vision and Pattern Recognition*, 2015, pp. 3431–3440.
 - [102] M. H. Wilkinson, T. Wijbenga, G. De Vries, M. A. Westenberg, Blood vessel segmentation using moving-window robust automatic threshold selection, in: *Proceedings 2003 International Conference on Image Processing (Cat. No. 03CH37429)*, Vol. 2, IEEE, 2003, pp. II–1093.
 - [103] T. Häikiö, R. Bertram, J. Hyönä, P. Niemi, Development of the letter identity span in reading: Evidence from the eye movement moving window paradigm, *Journal of Experimental Child Psychology* 102 (2) (2009) 167–181.
 - [104] J. Ohser, W. Nagel, K. Schladitz, The Euler number of discretized sets - on the choice of adjacency in homogeneous lattices, in: *Morphology of Condensed Matter*, Springer, 2002, pp. 275–298.
 - [105] S. Lichtenbaum, The Weil-étale topology on schemes over finite fields, *Compositio Mathematica* 141 (3) (2005) 689–702.
 - [106] T. Leinster, The Euler characteristic of a category, *arXiv preprint math/0610260*.
 - [107] C. Berger, T. Leinster, The Euler characteristic of a category as the sum of a divergent series, *Homology, Homotopy and Applications* 10 (1) (2008) 41–51.
 - [108] T. M. Fiore, W. Lück, R. Sauer, Finiteness obstructions and Euler characteristics of categories, *Advances in Mathematics* 226 (3) (2011) 2371–2469.
 - [109] S. van der Walt, J. L. Schönberger, J. Nunez-Iglesias, F. Boulogne, J. D. Warner, N. Yager, E. Goullart, T. Yu, Scikit-image: image processing in Python, *PeerJ* 2 (2014) e453. doi:10.7717/peerj.453. URL <https://doi.org/10.7717/peerj.453>
 - [110] E. H. van Brummelen, T. Demont, G. van Zwieten, An adaptive isogeometric analysis approach to elasto-capillary fluid-solid interaction, *International Journal for Numerical Methods in Engineering*.
 - [111] G. van Zwieten, J. van Zwieten, C. V. Verhoosel, E. Fonn, T. van Opstal, W. Hoitinga, *Nutils (version 5.0)* (2019). URL <http://doi.org/10.5281/zenodo.3243447>
 - [112] E. M. Garau, R. Vázquez, Algorithms for the implementation of adaptive isogeometric methods using hierarchical B-splines, *Applied Numerical Mathematics* 123 (2018) 58–87.
 - [113] M. Conti, C. Long, M. Marconi, R. Berchiolli, Y. Bazilevs, A. Reali, Carotid artery hemodynamics before and after stenting: A patient specific CFD study, *Computers & Fluids* 141 (2016) 62–74.
 - [114] P. A. Yushkevich, J. Piven, H. Cody Hazlett, R. Gimpel Smith, S. Ho, J. C. Gee, G. Gerig, User-guided 3D active contour segmentation of anatomical structures: Significantly improved efficiency and reliability, *Neuroimage* 31 (3) (2006) 1116–1128.